Journal Pre-proof

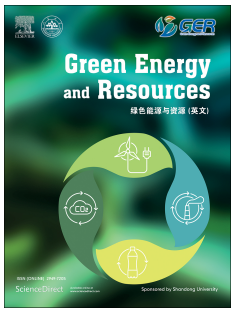

Flamelet/progress variable modelling of turbulent non-premixed cool flames of dimethyl-ether/methane mixtures

Weilin Zeng, Zeyang Pan, Xujiang Wang, Kai Hong Luo

PII: S2949-7205(25)00050-5

DOI: https://doi.org/10.1016/j.gerr.2025.100163

Reference: GER 100163

To appear in: *Green Energy and Resources*

Received Date: 29 September 2025

Revised Date: 4 November 2025

Accepted Date: 14 December 2025

Please cite this article as: Zeng, W., Pan, Z., Wang, X., Luo, K.H., Flamelet/progress variable modelling of turbulent non-premixed cool flames of dimethyl-ether/methane mixtures, *Green Energy and Resources*, https://doi.org/10.1016/j.gerr.2025.100163.

Study on Turbulent Non-Premixed Cool Flames of Dimethyl-Ether/Methane Mixtures

Method and Numerical Set-ups

Method: FPV-LES and Kinetic Modelling

LES Filtering:

$$\tilde{\psi}(\mathbf{t},\mathbf{x})=\frac{1}{\bar{\rho}}\int \rho(\mathbf{t},\mathbf{y})\,\psi(\mathbf{t},\mathbf{y})G(\mathbf{t},\mathbf{x},\mathbf{y};\Delta)\,d\mathbf{y}$$

FPV :

$$\frac{\partial(\bar{\rho}\tilde{Z})}{\partial t}+\frac{\partial(\bar{\rho}\tilde{u}_i\tilde{Z})}{\partial x_i}=\frac{\partial}{\partial x_i}\left[\bar{\rho}(D_z+D_t)\frac{\partial\tilde{Z}}{\partial x_i}\right]$$

$$\frac{\partial\left(\bar{\rho}\widetilde{Z^{\prime 2}}\right)}{\partial t}+\frac{\partial\left(\bar{\rho}\tilde{u}_i\widetilde{Z^{\prime 2}}\right)}{\partial x_i}=\frac{\partial}{\partial x_i}\left[\bar{\rho}(D_z+D_t)\frac{\partial\widetilde{Z^{\prime 2}}}{\partial x_i}\right]+2\bar{\rho}(D_z+D_t)\frac{\partial\tilde{Z}}{\partial x_i}\frac{\partial\tilde{Z}}{\partial x_i}-\bar{\rho}\tilde{\chi}$$

$$\frac{\partial(\bar{\rho}\widetilde{Yc})}{\partial t}+\frac{\partial(\bar{\rho}\tilde{u}_i\widetilde{Yc})}{\partial x_i}=\frac{\partial}{\partial x_i}\left[\bar{\rho}(D_z+D_t)\frac{\partial\widetilde{Yc}}{\partial x_i}\right]+\widetilde{\omega_{Yc}}$$

Cool Flame Configuration

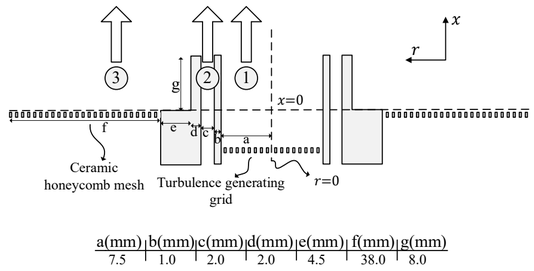

a(mm)	b(mm)	c(mm)	d(mm)	e(mm)	f(mm)	g(mm)
7.5	1.0	2.0	2.0	4.5	38.0	8.0

Schematic of the CARAT burner

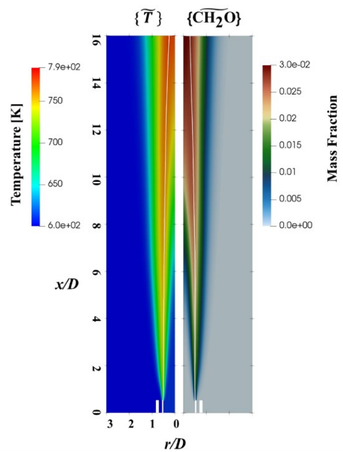

Simulated cool flame: model validation

Key findings

☐ Flame lifted with methane addition

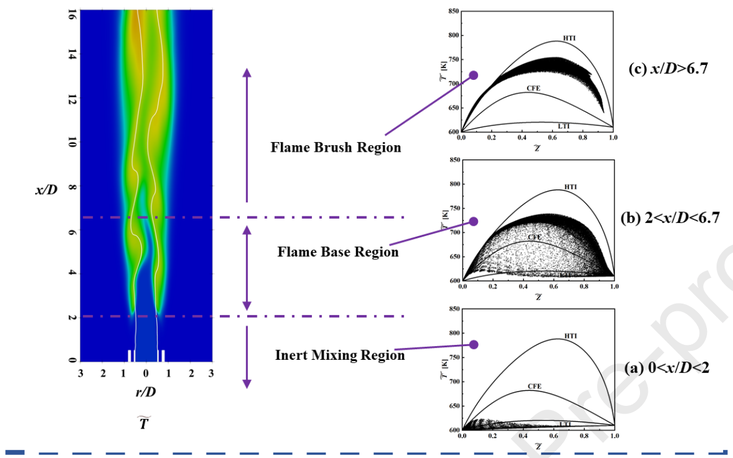

☐ Methane inhibits the low-temperature oxidation of DME

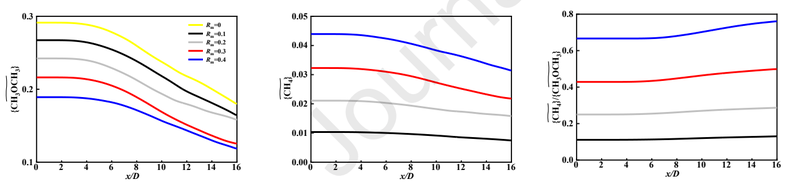

☐ Correlation between temperatures and key intermediate formation

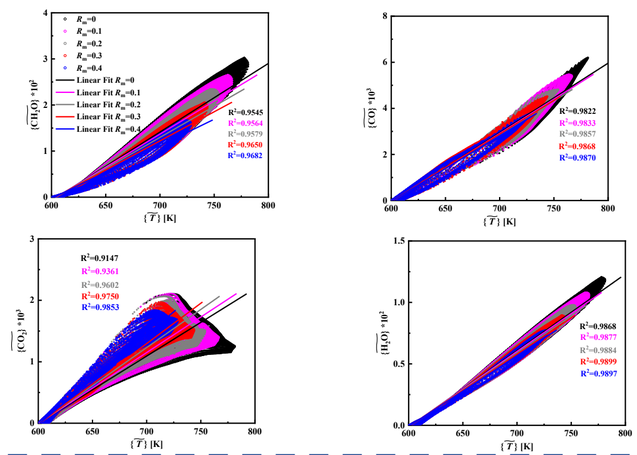

Mechanisms to explain

Flamelet S-curves

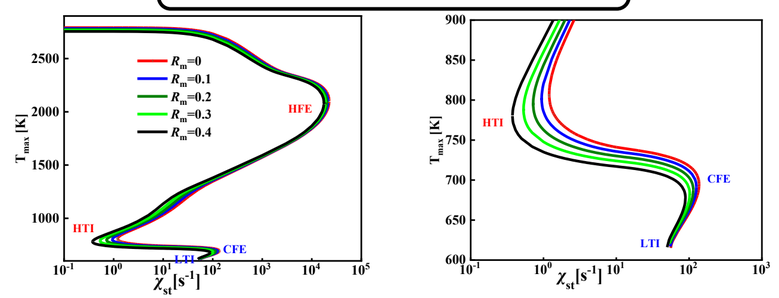

☐ methane addition decrease cool flame extinction limits

Reaction Flux Pathway Analyses

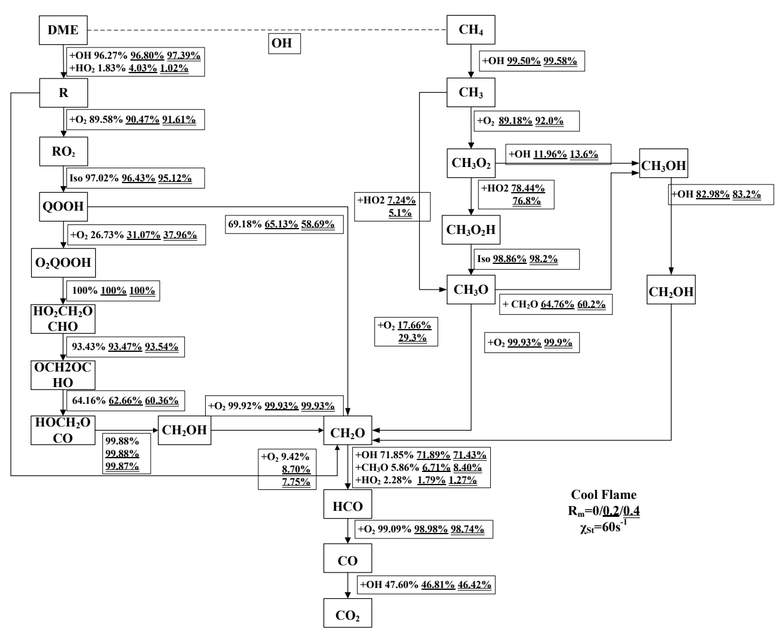

☐ CH4 competes with the DME H-abstraction reaction for OH radicals
☐ the reaction of QOOH <=> O2 + 2CH2O is significantly slowed down with the methane addition.

Flamelet/progress variable modelling of turbulent non-premixed cool flames of dimethyl-ether/methane mixtures

Weilin Zeng[a], Zeyang Pan[b], Xujiang Wang[b,*], Kai Hong Luo [c]

[a] School of Mechanical Engineering, Chengdu University, Chengdu, Sichuan 610106, PR China

[b] National Engineering Laboratory for Reducing Emissions from Coal Combustion, Shandong University, Jinan, Shandong 250061, PR China

[c] Department of Mechanical Engineering, University College London, Torrington Place, London WC1E 7JE, UK

[*]Corresponding Authors

Xujiang Wang

National Engineering Laboratory for Reducing Emissions from Coal Combustion, Shandong University

Jinan, Shandong 250061, PR China

Tel: +86-(0)531-88399372

Email: x.wang@sdu.edu.cn

Abstract

In present work, the turbulent non-premixed cool flames of dimethyl-ether (DME)/methane mixtures are studied within the framework of flamelet/progress variable modelling and chemical kinetic analyses. The numerical setup is based on the Princeton CARAT burner configuration, and the accuracy of the hpmech-V3.3 chemistry to model turbulent low-temperature combustion is validated against the reference experiments and DNS. The simulation results reveal that turbulent cool flame structures are modified (lifted) by methane addition owing to the decline of cool flame extinction limits. The different flame regions associated with differing thermochemical characteristics for the dual-fuel lifted cool flames are uncovered. The DME/methane consumption trends suggest that methane addition inhibits the DME low-temperature oxidation. Through the kinetic analyses, the mechanisms are identified to be two-fold: methane competes with the DME H-abstraction reaction for OH radicals and the reaction of QOOH <=> O_2 + 2CH_2O is significantly slowed down with the methane addition. The mechanisms also kinetically explain the finding that the formation of CH_2O, CO, CO_2 in cool flames decline in response to the increase of methane blending ratios. The correlation between temperature and key intermediate formation is discovered.

Keywords

DME/Methane; Turbulent cool flame; Large eddy simulation; Flamelet/progress variable; Flame lift.

Nomenclature

CARAT	Co-flow axisymmetric reactor-assisted turbulent	$C\chi$	The coefficient of χ
CCUS	The carbon capture, utilization, and storage	c_p	The isobaric specific heat capacity respectively
CFE	Cool flame extinction limit	D_t	The turbulent diffusivity
CI	Compression ignition	D_z	The molecular diffusivity of Z
DME	Dimethyl-ether	$\tilde{f}$	Filtered scalar
DNS	Direct numerical simulation	h_k	Specific enthalpy
FPV	Flamelet/progress variable	$P(Z)$	The probability density function
G	The filter kernel	$P(Yc\|Z$	The conditional probability density function
HCCI	Homogeneous charge compression ignition	p	The pressure
HTI	Hot-temperature ignition limit	Re_D	Reynolds number
LES	Large eddy simulation	R_m	The methane blending ratios
LTC	Low-temperature combustion	S_c	The Schmidt number
LTI	Low-temperature ignition limit	T	Temperature
PDF	Probability density functions	t	Represents time
QOOH	Hydroperoxyalkyl	u	The velocity vector
R	Hydrocarbon group	X	The mole fraction
R^2	The coefficients of determination in linear fits	x	The spatial coordinate
RCCI	Reactivity controlled compression ignition	Y_k	Chemical species mass fractions
RH	Alkyl hydrocarbon	Z	The mixture fraction
RMS	Root-mean-square	Δ	The filter size using the cubic root of cell volume.
RO_2	Alkyl peroxy	χ	Quantifies instantaneous scalar dissipation rate
SGS	Subgrid-scale	$\dot{\omega}_k$	Chemical reaction source term
		Y_C	Progress variable
–	Filtering operator	ρ	The density
{}	Time-averaged	~	Favre filtering

1. Introduction

In the recent decade, the global demand for energy diversity and the urgent imperative to mitigate greenhouse gas emissions have spurred the exploration of cleaner, more sustainable green fuels for next-generation internal combustion engines(Ge et al., 2025a, 2025b). Both Dimethyl ether (DME) and methane are recognized as attractive energy alternatives(Chai et al., 2016; Jiang et al., 2018; Lu et al., 2024; Moroshkina et al., 2025), since they can be widely obtained from biomass residues via catalytic conversion, organic waste by means of anaerobic digestion and CO_2 through the carbon capture, utilization, and storage (CCUS) technology(Ajayi-Banji and Rahman, 2024; Nakyai and Saebea, 2019; Tang et al., 2023; Uddin et al., 2020; L. Wang et al., 2023; Zhu et al., 2024). While DME is featured by excellent atomizing performance, low-temperature reactivity, simplicity of liquefaction and storage, superior thermal efficiency, and low-soot formation (Deng et al., 2014; Lu et al., 2024; Park and Lee,

2013; Wan et al., 2019; Zhou et al., 2025), CH_4 is characterised of low NOx and carbon dioxide emission, high auto-ignition temperature, low low-temperature reactivity, and short flammability limits, if applied alone to compression ignition (CI) engines(Gaipl et al., 2025; Li et al., 2025; Luo et al., 2023; Moroshkina et al., 2025). These combustion features have prompted consistent studies of DME/methane dual-fuel systems(Burke et al., 2015; Gao et al., 2020; Hashemi et al., 2019; Kaczmarek et al., 2021; Li et al., 2020; Lowry et al., 2011; Lu et al., 2024, 2021; Luo et al., 2017; Mohammad and Juhany, 2019; Nakamura et al., 2021; Porras et al., 2020; Sen et al., 2016; Wang et al., 2018; Yu et al., 2014; Zhang et al., 2022).

For the next-generation engine design, DME/methane binary fuels have also shown potential for feasibility in RCCI (Reactivity Controlled Compression Ignition) (Kokjohn et al., 2011), HCCI (Homogeneous Charge Compression Ignition)(Yao et al., 2009) and other promising low-temperature combustion (LTC) techniques. Jin et al. conducted an investigation into ignition behaviours of DME/methane blends with the RCCI regime by means of DNS (Direct Numerical Simulation). The multi-stage and multi-mode characteristics involving cool flames during the ignition stage are discovered (Jin et al., 2019). Ezoji et al. explored how DME addition influences the ignition timing in natural gas-fuelled HCCI engines. The findings showed that adding DME leads to the lower requirement for an injection temperature and the development of a dual-stage thermal release; meanwhile, the presence of dual fuels result in a rise in combustion chamber temperature and wall heat transfer (Ezoji et al., 2019). Banke et al. and Hegner et al. studied the use of DME/methane fuelled HCCI engines as reaction reactors to enable polygeneration. The outcome is favourable at fuel-rich conditions when equivalence ratios exceed 2 (Banke et al., 2019; Hegner et al., 2017). Desai et al. investigate the auto-ignition propagation speed of DME/methane blends in stratified combustion. The inherent impacts of stratification on the low- and high-temperature chemistry are investigated for the instructions of dual-fuel RCCI engines (Desai et al., 2020). Such dual-fuel approaches have been proposed as a promising LTC technique to enhance thermal efficiency without compromising low emissions, which highlights the significance of low-temperature chemistry or cool flames(Ju, 2021; Ju et al., 2019).

Cool flames(Ju, 2021; Ju et al., 2019) are intricately linked to ignition processes(Jin et al., 2019; Reuter et al., 2016; Zhang and Ju, 2020; Zhao et al., 2016), combustion rate(Benteux et al., 2025; Liang and Law, 2017), extinction limits(Benteux et al., 2025; Reuter et al., 2017; Xu et al., 2022), engine knocking(Amann et al., 2011; Bradley and Kalghatgi, 2009; Qi et al., 2017; Sun et al., 2015), and pollutant formation(Dbouk et al., 2025; Reuter et al., 2018; Yan et al., 2022a). In diesel engines, for instance, autoignition and autoignition-assisted flame

propagation are the primary phenomena in combustion. Autoignition is triggered by first-stage ignition and the subsequent shift to a cool flame. The cool flames then spread from lean to rich mixtures. Afterward, second-stage (hot) ignition takes place in fuel-rich regions, where turbulent hot flames are established and spread back from the rich mixture toward the stoichiometric mixture location(Murakami et al., 2021). Recent research shows DME exhibits distinct LTC and cool flame characteristics: 1) High low-temperature oxidation reactivity: It easily triggers cool flames at 500–800 K (lower than conventional fuels like diesel), and there is no need for high compression to ignite; 2) Key cool flame reaction pathway: Dominated by "RH→R→RO_2→QOOH" reactions. QOOH (hydroperoxyalkyl radical) is the core intermediate, which decomposes to produce CH_2O (formaldehyde) and releases moderate heat (not enough for hot ignition); 3) Cool flame products: Mainly incomplete oxidation products (CH_2O, CO) instead of final CO_2/H_2O, with low heat release compared to hot flames(Z. Wang et al., 2023; Yan et al., 2022b). Comparatively, methane has weak LTC features, as its strong C-H bonds require higher temperatures to initiate low-temperature oxidation, making it hard to trigger reactions at typical "cool flame temperatures" (500–800 K) at atmosphere or moderate pressures or without mixing with reactive fuels like DME(Wang and Gou, 2019).

Since cool flames in practical engines often occur at turbulent atmospheres, it is of significance to study the interaction between cool flames and turbulence. However, limited research literature focuses on the investigations of DME/methane cool flame dynamics, especially from the turbulent combustion modelling perspective. Cool flames are characteristic of low temperature chemistry behaviours that need detailed chemical mechanisms in turbulent simulation. Manifolds-based models such as FPV (Flamelet/Progress Variable) (Ihme et al., 2005; Pierce and Moin, 2004) and flamelet-generated manifolds (OIJEN and GOEY, 2000; van Oijen et al., 2016), building themselves on the flamelet concept of depicting a turbulent flame as a collection of laminar flamelets(Peters, 1988), enable an effective entry to complex thermochemistry at a substantially reduced computational cost. To examine the feasibility of reduced-order manifold modeling in turbulent cool flames, Novoselov et al. have carried out high-fidelity DNS of non-premixed DME cool flames coupled with unsteady isotropic turbulence (Novoselov et al., 2019a). It is found that such cool flames can be suitably represented by steady flamelets. To continue this work, Novoselov et al. have conducted experiments and DNS investigations into turbulent non-premixed DME cool flames established on the Princeton CARAT (Co-flow Axisymmetric Reactor-Assisted Turbulent) burner (Novoselov et al., 2019b). The findings strengthen the conclusion by comparing conditional averages, rather than

just analyzing instantaneous scalars, that manifold models can characterize turbulent non-premixed cool flames. Within the scope of LES (Large Eddy Simulation), the first author and co-workers have carried out an LES on the same Princeton CARAT burner with the steady laminar flamelet method(Xiong et al., 2023) and FPV(Zeng et al., 2026). The discoveries reveal that reduced-order manifolds modelling can effectively replicate the averaged values and RMS (Root Mean Square) tendencies of temperature, mixture fraction, and formaldehyde. In spite of the merits of manifolds-based models, their application to turbulent DME/ methane cool flames hasn`t been reported in the literature.

Furthermore, the modelling of cool flames requires precise chemistry. To characterize DME/ methane low-temperature oxidation reactions, the hpmech-V3.3 chemical scheme(Reuter et al., 2018) has been established. Tailored to the reactivity at both cool and hot flames, this dual-fuel chemistry is rigorously validated against a comprehensive suite of experimental targets: counterflow flames, homogeneous reactors, and plug flow reactors. It favourably delivers a well-verified chemistry scheme for simulating turbulent DME/methane cool flames.

Based on the discussions above, the current work intends to study the turbulent non-premixed cool flames of dimethyl-ether (DME)/methane mixtures with the approaches of both LES and chemical kinetic analyses. This paper is arranged in the following manner: Section 2 outlines the specifics of the computational methodologies. Section 3 describes flame configurations alongside computational setups. Section 4 delineates the results and discussion about the modelling accuracy of the employed chemistry and the effects of methane blending ratios on turbulent non-premixed methane/DME cool flames. Section 5 offers a synthesis of the research findings.

2. The numerical methods

2.1 LES

In LES, large-scale eddies within the flow field are directly resolved, whereas subgrid-scale turbulence and chemistry effects are addressed through modeling(Smagorinsky, 1963). Scale segregation is facilitated through low-pass filtering of fluid domain variables. In combustion modelling, the mass-weighted Favre filtering scheme is actually implemented as follows:

$$\widetilde{\psi}(t,\mathbf{x})=\frac{1}{\overline{\rho}}\int \rho(t,\mathbf{y})\,\psi(t,\mathbf{y})G(t,\mathbf{x},\mathbf{y};\Delta)\,d\mathbf{y} \tag{1}$$

Here, $\bar{}$ is the filtering operator, $\tilde{}$ means Favre filtering, t represents time, x denotes the spatial coordinate, ρ is the density, and G stands for the filter kernel. Δ is the filter size using the cubic root of cell volume.

By applying the filtering operation to the Navier-Stokes equations under the low-Mach numbers assumption, the governing equations of LES can be formulated as

Continuity:

$$\frac{\partial \bar{\rho}}{\partial t} - \frac{\partial \bar{\rho}\widetilde{u_j}}{\partial x_j} = 0 \tag{2}$$

Momentum:

$$\frac{\partial(\bar{\rho}\widetilde{u_i})}{\partial t} + \frac{\partial\left(\bar{\rho}\widetilde{u_i}\widetilde{u_j}\right)}{\partial x_j} = -\frac{\partial \bar{p}}{\partial x_i} + \frac{\partial}{\partial x_j}[\bar{\tau}_{ij} - \bar{\rho}(\widetilde{u_i u_j} - \widetilde{u_i}\widetilde{u_j})] \tag{3}$$

Here, ρ denotes the density, u represents the velocity vector, p stands for the pressure. Given that the residual stress tensor $\bar{\rho}(\widetilde{u_i u_j} - \widetilde{u_i}\widetilde{u_j})$ remains unresolved, a dynamic k-equation subgrid-scale model(Kim and Menon, 1995) is employed for its representation. This eddy viscosity model utilizes a formulated transport equation to assess the behavior of k, with a dynamic procedure applied to settle the coefficients.

2.2 FPV model

The FPV model is established upon the flamelet equations(Pierce and Moin, 2004). In these equations, a turbulent non-premixed flame is depicted as a collection of laminar flamelets(Peters, 1988). In terms of turbulent cool flames, the steady flamelet equations (Equations 4 and 5) are formulated under the presumption of unity Lewis numbers. It is extensively employed in high-temperature flames at large Reynolds numbers, in which viscosity is elevated by thermal gradients within the flame zone by a factor of 10, contributing to the same decade-scale attenuation of the Reynolds number(Novoselov et al., 2019b). In spite of their much smaller Reynolds numbers, the validity for turbulent cool flames is supported in the DNS studies(Novoselov et al., 2019a, 2019b), owing to minimal variations in temperature and viscosity, consequently suppressing Reynolds number fluctuations(Novoselov et al., 2019b).

$$\frac{1}{2}\rho\chi\frac{\partial^2 Y_k}{\partial Z^2} + \dot{\omega}_k = 0 \tag{4}$$

$$\frac{1}{2}\rho\chi\left(\frac{\partial^2 T}{\partial Z^2} + \frac{1}{c_p}\frac{\partial c_p}{\partial Z}\frac{\partial T}{\partial Z}\right) - \frac{1}{c_p}\sum_{k=1}^{n} h_k\dot{\omega}_k = 0 \tag{5}$$

Here, Y_k, T and c_p denote chemical species mass fractions, temperature and the isobaric specific heat capacity respectively; h_k and $\dot{\omega}_k$ correspond to specific enthalpy and chemical reaction source term. χ quantifies

instantaneous scalar dissipation rate. *Z*, representing the mixture fraction, adheres to the definition by Bigler(Bilger, 1989).

Additional flow field scalars like species mass fractions can be retrieved through interpolation in the pre-generated laminar flamelet database, with *Z* and Y_C serving as manifolds-based parameters: *f=f(Z,Yc)* .

In LES of turbulent combustion, the filtered variable $\tilde{f}$ is typically reconstructed through presumed probability density functions (PDFs) of the filtered quantities $\widetilde{Y_C}$ and $\widetilde{Z}$.

$$\tilde{f} = \iint f(Z,Yc)\tilde{P}(Z,Yc)dZdYc \tag{6}$$

$$\tilde{P}(Z,Yc) = P(Yc|Z)P(Z) \tag{7}$$

Following the references(Ihme et al., 2005; Ihme and Pitsch, 2008a; Pierce and Moin, 2004; Xiong et al., 2023), *P(Z)* adopts the beta distribution (*β*-PDF). Under the state-space independence assumption(Pierce and Moin, 2004), the conditional probability density function $P(Yc|Z)$ can be mathematically represented by a Dirac delta function. Consequently, a tri-variate flamelet look-up table $\tilde{f} = f(\tilde{Z}, \widetilde{Yc}, \widetilde{Z''^2})$ can be constructed for turbulent flames. The library-constructing parameters are solved by their individual transport equations:

$$\frac{\partial(\overline{\rho}\tilde{Z})}{\partial t} + \frac{\partial(\overline{\rho}\widetilde{u_i}\tilde{Z})}{\partial x_i} = \frac{\partial}{\partial x_i}\left[\bar{\rho}(D_z + D_t)\frac{\partial \tilde{Z}}{\partial x_i}\right] \tag{8}$$

$$\frac{\partial\left(\overline{\rho}\widetilde{Z''^2}\right)}{\partial t} + \frac{\partial\left(\overline{\rho}\widetilde{u_i}\widetilde{Z''^2}\right)}{\partial x_i} = \frac{\partial}{\partial x_i}\left[\bar{\rho}(D_z + D_t)\frac{\partial \widetilde{Z''^2}}{\partial x_i}\right] + 2\bar{\rho}(D_z + D_t)\frac{\partial \tilde{Z}}{\partial x_i}\frac{\partial \tilde{Z}}{\partial x_i} - \overline{\rho}\tilde{\chi} \tag{9}$$

$$\frac{\partial(\overline{\rho}\widetilde{Yc})}{\partial t} + \frac{\partial(\overline{\rho}\widetilde{u_i}\widetilde{Yc})}{\partial x_i} = \frac{\partial}{\partial x_i}\left[\bar{\rho}(D_z + D_t)\frac{\partial \widetilde{Yc}}{\partial x_i}\right] + \widetilde{\omega_{Yc}} \tag{10}$$

D_z represents the molecular diffusivity of *Z*, postulated to be equivalent to the thermal diffusivity under unity Lewis number assumption, and D_t denotes the turbulent diffusivity, computed through the expression $S_c = \mu_t / (\rho D_t)$(Gicquel et al., 2012). The Schmidt number S_c commonly spans a range from 0.4 to 1(Pant et al., 2019; See and Ihme, 2015). In current work, a value of 1 is employed, based on the sensitivity analysis in turbulent cool flame modelling reported in the prior study(Xiong et al., 2023). The filtered scalar dissipation rate adheres to the formulation following (Gao et al., 2020; Ihme et al., 2012a, 2012b; Ihme and Pitsch, 2008a), which breaks down the term into resolved-scale and subgrid-scale (SGS) components:

$$\tilde{\chi} = 2D_Z\left|\nabla\tilde{Z}\right|^2 + 2D_t\frac{C_\chi}{2\Delta^2}\widetilde{Z''^2} \tag{11}$$

where the coefficient $C\chi$ is given a value of 2, consistent with (Gao et al., 2020; Ihme et al., 2012a, 2005; See and Ihme, 2015; Xiong et al., 2023).

Numerically, the FPV-LES framework is implemented in the open-source platform of OpenFOAM (Weller et al., 1998). Its applicability to turbulent cool flames has been validated against the experiments and DNS of the Princeton CARAT burner (Novoselov et al., 2019b) in the previous study (Zeng et al., 2026).

3. Flame configurations and computational setups

3.1. Experiment description

The computational setup corresponds to the turbulent non-premixed cool flame configuration on the CARAT burner at Princeton University(Novoselov et al., 2019b), and the burner schematic is shown in Figure 1. The burner is equipped with three concentric flow paths: A central fuel nozzle (Stream 1) featuring a diameter of D=15mm, an annular pilot channel (Stream 2) supplying 2mm radial clearance around the primary outlet, and an external co-flow conduit (Stream 3) for flow stabilisation. The fuel mixture in Stream 1 comprises N_2, acetone, and DME with respective volume fractions of 78%, 2%, and 20%. To maintain flame stability while inducing controlled turbulence at a Reynolds number of Re_D=911 ($\bar{U}$=2.5m/s, U_{RMS}=0.42m/s) based on D, two perforated plates are incorporated upstream of the nozzle exit at Stream 1. Stream 2 delivers pure oxygen at a velocity of U_2 = 1 m/s, while Stream 3 supplies ambient air with a reduced velocity (U_3= 0.5 m/s) to minimize flow disturbances. All fluid inlets are maintained at 600 K through preheating.

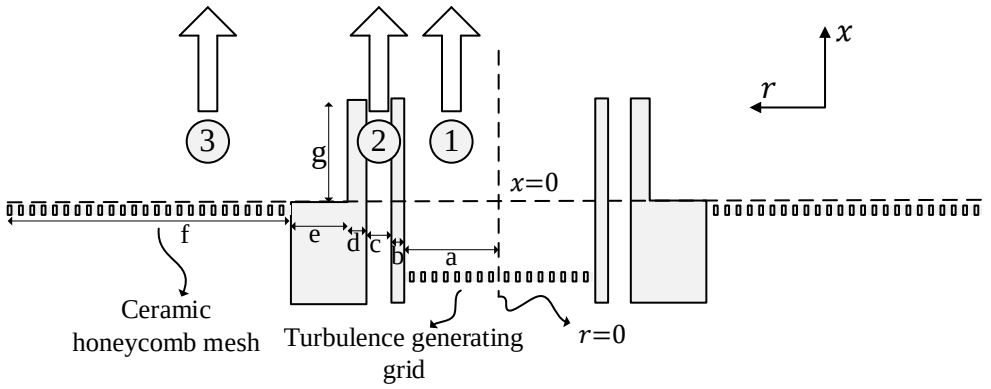

a(mm)	b(mm)	c(mm)	d(mm)	e(mm)	f(mm)	g(mm)
7.5	1.0	2.0	2.0	4.5	38.0	8.0

Figure 1. Schematic of the CARAT burner. A photograph of the burner prototype is available in the referenced

study (Novoselov et al., 2019b).

3.2. Computational domain and Mesh allocation

Numerical computations are carried out above the x= 0 reference line (Figure 1). The cylindrical simulation domain is configured as follows: (1) A radial dimension of 6D is selected to minimize lateral boundary effects; (2) An axial dimension of 16D is implemented to accommodate flame propagation and thermal expansion of downstream. The computational mesh employs a polar coordinate system with a central square region (O-type grid) to prevent overly dense meshing along the axis.

The specific grid allocation consists of 81 tangential, 48 azimuthal, and 200 axial cells, as well as the O-grid region covering 12×12 cells. Mesh stretch is deliberately applied in both axial and tangential orientations to address turbulent flow non-uniformity at the inlet region and sharp gradients arising in the vicinity between Stream 1 and Stream 2. The grid independence has been verified in the same CARAT burner in the earlier studies(Xiong et al., 2023; Zeng et al., 2026). The specific grid distribution is shown in Figure 2.

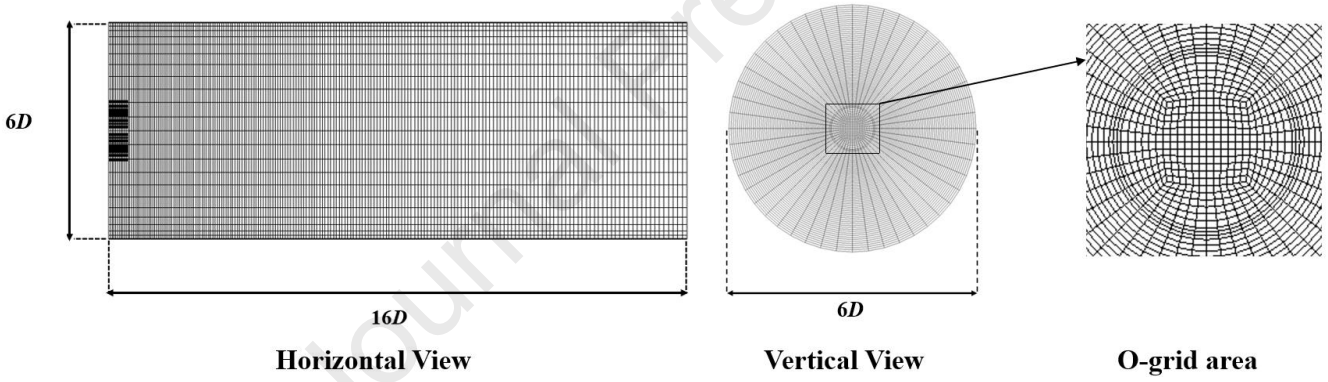

Figure 2. The grid allocation(Xiong et al., 2023).

3.3 Boundary conditions and chemistry schemes

To represent DME/methane oxidation reactions, the hpmech-V3.3 chemical scheme(Reuter et al., 2018), comprising 130 species and 876 reactions, is employed in turbulent cool flame modelling. Tailored to the reactivity at both low and high temperatures, this dual-fuel chemistry is rigorously validated against a comprehensive suite of experimental targets: counterflow flames, homogeneous reactors, and plug flow reactors. The progress variable is defined as $Y_C = Y_{CO2} + Y_{H2O} + Y_{CO} + Y_{H2}$, following (Ihme and Pitsch, 2008a, 2008b; Pant et al., 2019; See and Ihme, 2015; Zeng et al., 2026).

On the inlets, inflow turbulence at Stream 1 is generated with the random spots method(Kornev and Hassel, n.d.), employing the mean velocities, Reynolds stress tensor, and integral length scales corresponding to the

experimental conditions. It has been applied across multiple LES studies and has exhibited the capability to reproduce coherent vortices(Chen et al., 2020; Guo et al., 2018; Wu, 2017; Zhang et al., 2024). Streams 2 and 3 are assigned with experimentally measured bulk flow velocities. Lateral boundaries adopt free-slip conditions, and non-reflective treatment is enforced at the domain exit plane. Nozzle walls are defined with adiabatic and no-slip.

The specific scalar boundary conditions are detailed in Table 1. Before investigating the dual fuels, the accuracy of the hpmech-V3.3 chemical scheme(Reuter et al., 2018) to model turbulent cool flames is scaled against the experiments and DNS of the CARAT burner (Novoselov et al., 2019b). Notably, DNS employs the different chemistry of the Wang model(Wang et al., 2015), without the validated low-temperature CH_4 sub-mechanisms. Scalar boundary profiles adopt uniform distributions from experimental data, with Stream 1 composition modified to X_{N2}=0.8 and $X_{CH3OCH3}$=0.2 (excluding the tracer acetone presented experimentally). This is identical to DNS configurations(Novoselov et al., 2019b). To be particularly noted, slight variation exists in thermal and species boundary implementations between numerical and experimental configurations. The original three-stream combustion system (distinct compositions in Stream 2: pure O_2; Stream 3: air) is computationally simplified to a two-stream model by specifying identical oxidizer (pure O_2) for both Streams 2 and 3. This simplification, justified by DNS evidence of minimal co-flow composition impact(Novoselov et al., 2019b), reduces computational expense associated with triple-stream interaction modeling. The validity of this assumption in LES is also proved in the previous analysis(Xiong et al., 2023; Zeng et al., 2026). In line with the DNS configuration, the temperature setting at the fuel inlet (Stream 1) is elevated to 610 K. This temperature raise aims to replicate wall heat transfer effects and prevent flame detachment, a phenomenon observed under 600 K inlet conditions in the DNS(Novoselov et al., 2019b). R_m=0 (the methane blending ratios R_m, defined as $R_m = X_{CH4}/(X_{CH4} + X_{DME})$) in Table 1 corresponds to the validation simulation.

Table 1. The inflow species boundary condition specifications

Abbreviation	Method	Stream 1				Stream 2	Stream 3
		Composition	R_m	X_{fuel}	X_{N2}		
Experiment (Novoselov et al., 2019b)	**Experiment**	DME (18%vol) /Acetone(2%vol)/N_2	0	0.2	0.8	O_2	Air
DNS (Novoselov et al., 2019b)	**DNS**	DME /N_2	0	0.2	0.8	O_2	Air

R_m=0	**FPV-LES**	DME /N_2	0	0.2	0.8	O_2	O_2
R_m=0.1	**FPV-LES**	CH_4/ DME / N_2	0.1	0.2	0.8	O_2	O_2
R_m=0.2	**FPV-LES**	CH_4/ DME / N_2	0.2	0.2	0.8	O_2	O_2
R_m=0.3	**FPV-LES**	CH_4/ DME / N_2	0.3	0.2	0.8	O_2	O_2
R_m=0.4	**FPV-LES**	CH_4/ DME / N_2	0.4	0.2	0.8	O_2	O_2

To isolate the effects of methane addition, the mole fraction of the fuel mixture on Stream 1 is fixed at X_{fuel}=0.2, and the methane blending ratios in the fuel mixture vary from R_m=0 to R_m=0.4. The thermal boundaries for Streams 2 and 3 are kept 600K, the same as the experiments.

3.4. Numerical aspects

The filtered governing equations are numerically resolved through a finite-volume discretization framework. Velocity-pressure coupling is resolved via the PIMPLE algorithm, with temporal discretization handled by the second-order implicit Crank–Nicolson method. The time step is adjusted adaptively in real time to maintain the Courant number at a value of 0.06. Spatial reconstruction adopts a hybrid approach: convective terms are discretized using multidimensional limited linear cell interpolation, whereas diffusive terms combine central differencing with gradient face interpolation. Statistical averaging processes cover seven flow-through periods, defined by the bulk velocity of Stream 1. Prior to data acquisition, four preliminary flow-through cycles are simulated to achieve fully established flow fields.

LES is carried out on the BSCC-A6 hypercomputing system with up to 320 2.35 GHz processors, while flamelet solutions and chemical kinetic analyses are calculated with the software FlameMaster (H.Pitsch, n.d.) on local serial nodes.

4 *Results and discussion*

4.1. Chemical scheme accuracy

In this part, the accuracy of the hpmech-V3.3 chemical scheme(Reuter et al., 2018) to model turbulent cool flames is scaled against the experiments and DNS of the CARAT burner (Novoselov et al., 2019b). Figure 3 presents the time-averaged filtered temperature and formaldehyde mass fraction contours in central longitudinal

sections at R_m=0 from the FPV-LES using the hpmech-V3.3 chemistry, along with the solid iso-lines representing Z_{st}=0.622. As can be seen, stabilized cool flames are attached near the burner tip, featuring the burning temperature varying between 600K and 790K and the substantial $\widetilde{CH_2O}$ formation up to 3 % mass fraction. To compare against experiments and DNS(Novoselov et al., 2019b), the radial profiles of temporally averaged temperature, mixture fraction, and formaldehyde mass fraction calculated by LES are illustrated in Figure 4. To mitigate measurement noise, experimental datasets are obtained within a confined spatial range (x/D=1.5–2.0) and averaging is performed in the axial direction(Novoselov et al., 2019b). The same procedures are implemented on the DNS and LES results for contrasting. Experimental measurements in both positive and negative radial directions were not averaged; instead, they are presented individually to highlight the degree of variability in the experiment. In terms of $\widetilde{T}$ and $\widetilde{CH_2O}$ mean distributions, the FPV predictions show closer agreement with DNS, while larger overestimations against experimental data are noted in the normalized radial interval of $0.7 < r/D < 1.3$. Regarding $\widetilde{Z}$ mean profiles, the LES predictions match closely with both DNS and experiments across most of the radial domain, with a slight overestimation on the fuel-rich side ($r/D < 0.9$). Given that the LES setup raises the fuel inlet temperature to 610 K (consistent with DNS), the FPV-LES captures reasonably well the qualitative and quantitative trends in line with DNS.

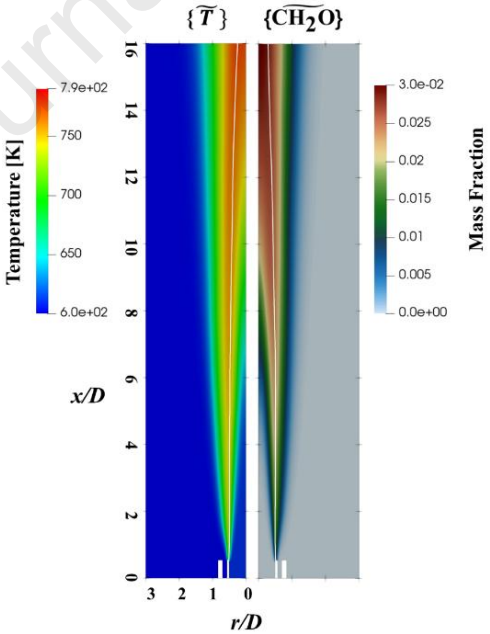

Figure 3 Time averaged filtered temperature and formaldehyde contours in central longitudinal sections. The curly brackets {} means time-averaged here and in subsequent sections.

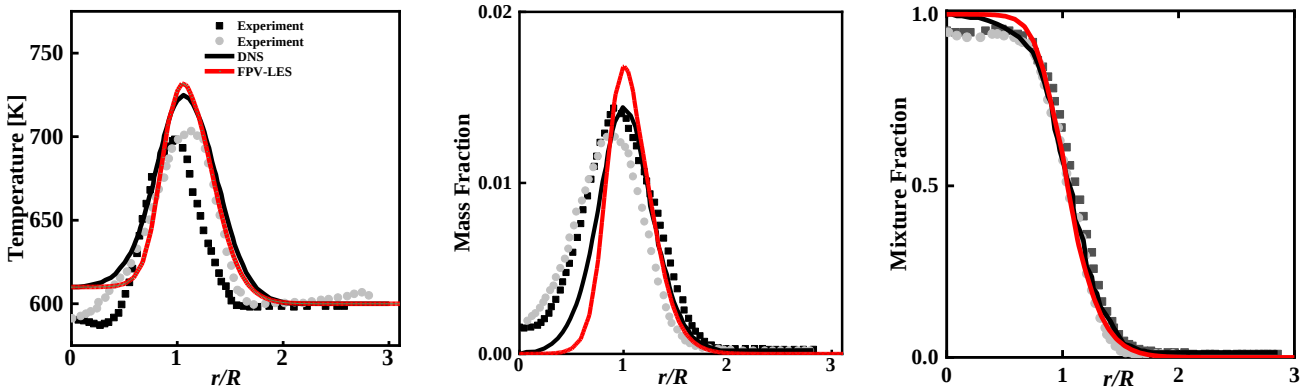

a) $\{\widetilde{T}\}$ b) $\{\widetilde{CH_2O}\}$ c) $\{\widetilde{Z}\}$

Figure 4 Comparison of temporally averaged temperature, mixture fraction and formaldehyde between LES, DNS(Novoselov et al., 2019b) and experiments(Novoselov et al., 2019b).

The comparison of turbulent scalar fluctuations in mixture fraction and formaldehyde mass fractions is quantified by means of their respective root-mean-square (RMS) profiles, as illustrated in Figure 5. Concerning the $\widetilde{CH_2O}$ variance, the LES simulations demonstrate qualitative concordance with experiments and DNS, but in quantity, the discrepancy is two-fold. Firstly, DNS yields notably higher values at the centerline, as opposed to the almost zero predictions from LES. Secondly, a minor secondary peak is detected in LES within $1<r/D<1.3$, where DNS exhibits a flat profile. There are three causes: firstly, to align with experimental configurations, DNS implements an extra simulation of a periodic box for Stream 1's inflow turbulence, while the LES in the present study adopts a simpler synthetic turbulence generation approach(Kornev and Hassel, n.d.); Second, the filtered formaldehyde mass fraction for LES is obtained indirectly by looking up tables from FPV flamelet libraries, whereas in DNS, this scalar is directly solved by means of transport equations; Thirdly, the original three-stream combustion system (distinct compositions in Stream 2: pure O_2; Stream 3: air) in experiments and DNS is computationally simplified to a two-stream model in LES by specifying identical oxidizer (pure O_2) for both Streams 2 and 3. The different O_2 content setup in the co-flow could influence the variance trend of CH_2O near the Stream 3. The evidence and further explanation can be found in the Supplementary Material.

The second reason is supported by comparing the $\widetilde{Z}$ RMS in Figure b. The LES results display strong agreement with DNS in quality and quantity. The subtle disparity exists in the peak prediction: the FPV-LES yields a peak over-prediction of 0.02. Thus, a significant enhancement in $\widetilde{Z}$ RMS prediction is realized by LES over $\widetilde{CH_2O}$ RMS. As a manifold-constructing parameter, $\widetilde{Z}$ is directly solved by its governing equation in FPV-LES,

analogous to the resolution of CH_2O species transport equations in DNS.

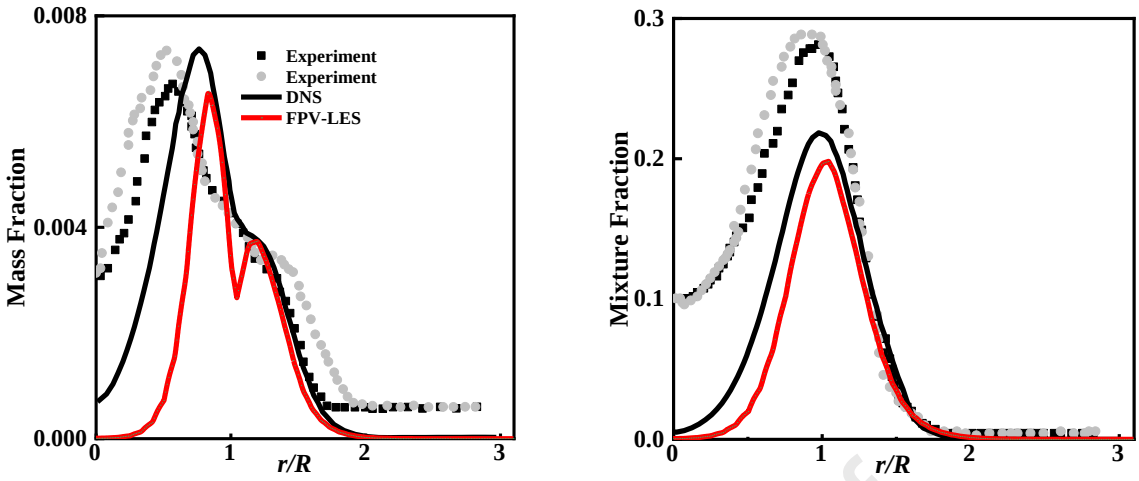

a) $\widetilde{CH_2O}_{RMS}$ b) $\widetilde{Z}_{RMS}$

Figure 5 Comparison of mixture fraction and formaldehyde variance between LES, DNS(Novoselov et al., 2019b) and experiments(Novoselov et al., 2019b).

On the whole, FPV-LES with the hpmech-V3.3 chemistry yields results that agree reasonably well with DNS data, confirming the accuracy of the dual-fuel chemical mechanism to reproduce turbulent cool flames.

4.2 Flame structures

The LES-predicted instantaneous and time-averaged filtered temperature contours in central longitudinal sections at R_m=0-0.4 are shown in Figure 9, along with the white solid lines representing the iso-contours of the stoichiometric mixture fraction. As can be seen, stabilized cool flames are anchoring near the burner tip at lower methane proportions of R_m=0-0.2, where burning temperatures span from 610K to 790K. As R_m increases to 30%, the cool flames are becoming lifted off. Looking at Figure 6d, a noticeably cold, non-reacting region is found within a height of 2D extending from x=0, implying that fuel and oxidizer mix inertly without significant reactions or heat release. Immediately downstream this inert mixing region, the flame base displays a diffusion-dominated flame structure, with a thin reaction layer separating fuel and oxidizer streams. This transition zone persists from x/D=2 to 6.7, until a turbulent, brush-shaped flame spreads downstream, featuring large-scale vortices. The same morphological feature of a lifted diffusion cool flame is also detected in the case of R_m=0.4 (Figure 6e). In contrast, the lift-off height, defined as the axial distance from the nozzle exit to the flame base, is larger (roughly 3.3D), and the transition zone is longer (from x/D=3.8 to 9.8).

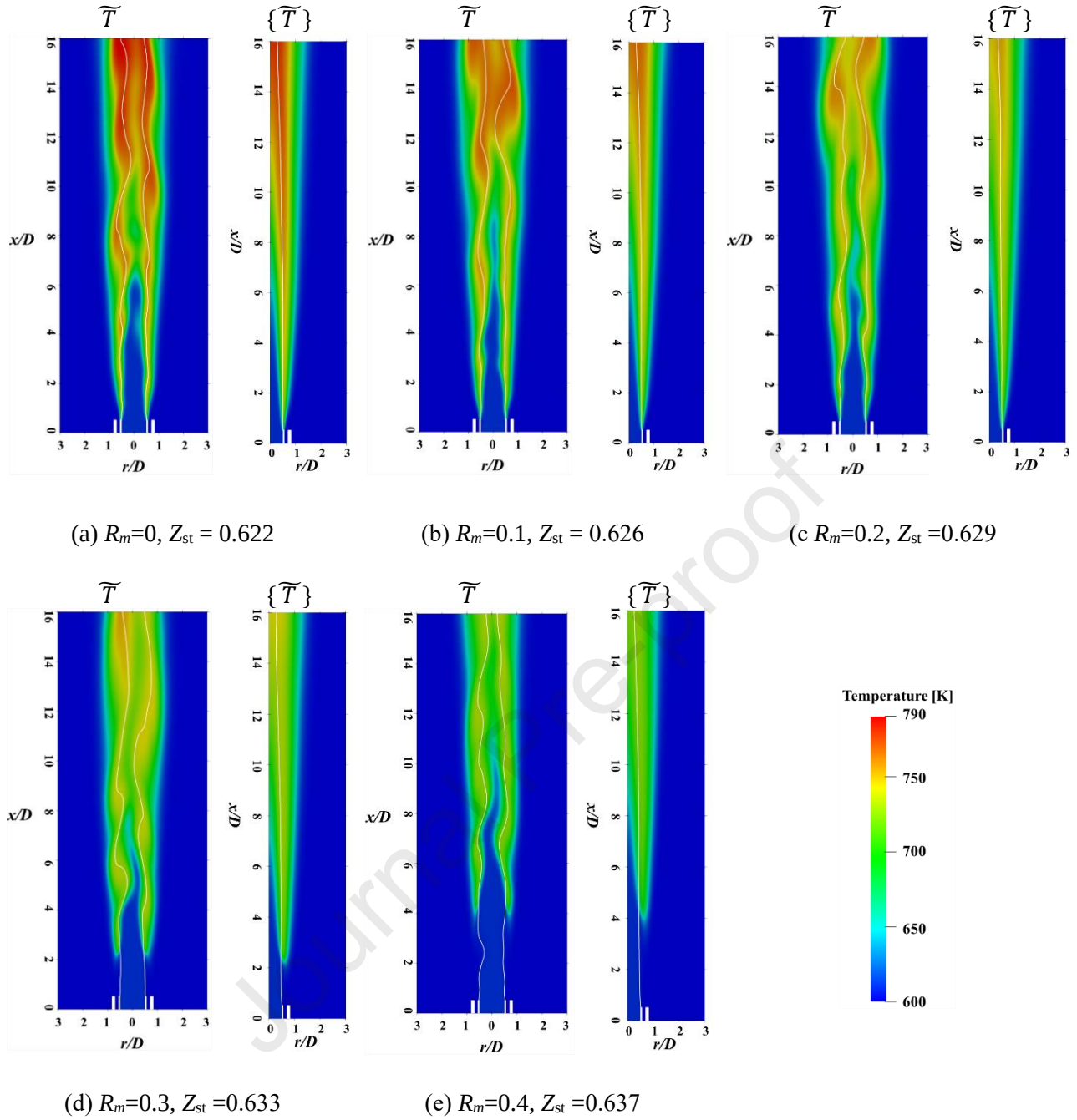

(a) R_m=0, Z_{st} = 0.622 (b) R_m=0.1, Z_{st} = 0.626 (c R_m=0.2, Z_{st} =0.629

(d) R_m=0.3, Z_{st} =0.633 (e) R_m=0.4, Z_{st} =0.637

Figure 6 Instantaneous and averaged filtered temperature contours in central longitudinal sections under different R_m.

To elucidate the impacts of methane addition on the cool flame structures, Figure 7 displays the scattered temperature maximums in each single laminar flamelet solution at different stoichiometric scalar dissipation rates for different methane blending ratios by FlameMaster. Notably, LTI denotes low-temperature ignition limit, CFE cool flame extinction limit, HTI hot-temperature ignition limit, and HFE hot flame extinction limit. As it presents, the temperature profile in the S-curve falls as methane blending ratios go up. It is in accordance with the findings

in the study(Reuter et al., 2018), that the heat release of methane/DME cool flames is primarily governed by the low-temperature chemistry of DME. This accounts for the observations in Figure 9 that, with the increase of methane blending ratios, the temperature distributions exhibit an overall decrease in both instantaneous and time-averaged temperature distributions.

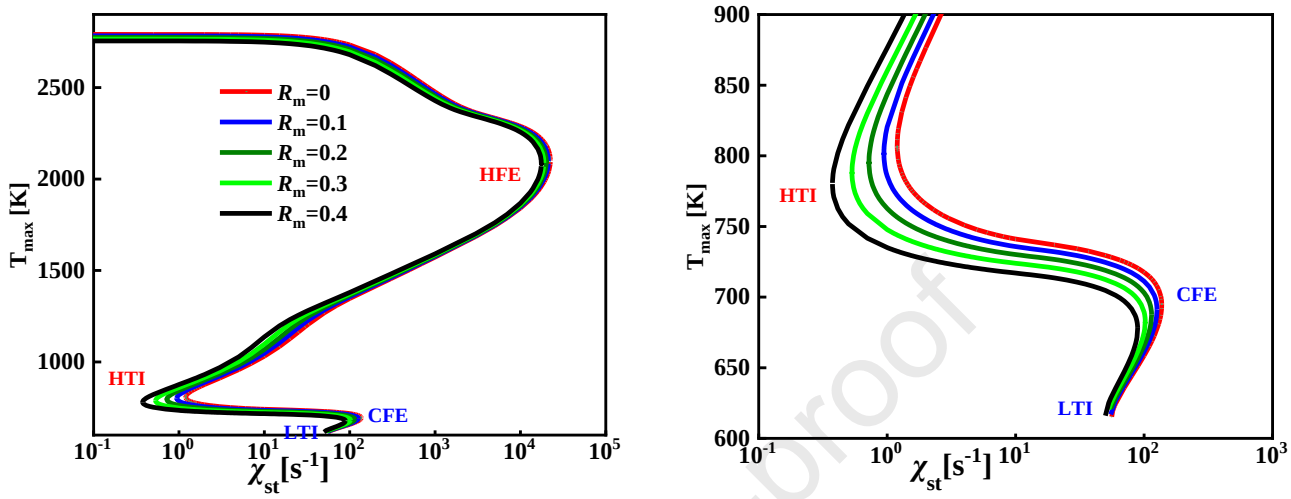

(a) Full view (b) Zoomed-in view

Figure 7 The scattered temperature maximums in each single laminar flamelet solution at different stoichiometric scalar dissipation rates for various R_m.

Meanwhile, Figure 7 also demonstrates that the CFE limits drop in response to the increase of methane blending ratios. It indicates that with identical inlet velocity settings, fuel with larger methane adding (R_m=0.3 and R_m=0.4) are more prone to extinguishing in the high-strain-rate regions adjacent to the nozzle, driving the flame into stabilizing further downstream in zones with lower strain rates (becoming lifted). Moreover, as the blending ratio rises, the lift-off height increases (R_m=0.4> R_m=0.3), demonstrating the impact of methane addition on the flame lift through CFE limit decline.

Figure 8 depicts instantaneous scatter plots of $\widetilde{T}$ as functions of $\widetilde{Z}$ under different R_m. The sampling space consists of all spatial cells throughout the entire computational domain, at a simulation time when turbulent flames are sufficiently established for every methane blending ratio. The instantaneous filtered temperature contours in central longitudinal sections corresponds to Figure 6. The solid lines within the figure correspond to the laminar flamelet solutions at different flame limits (LTI, CFE and HTI) of the S-curves in Figure 7. As observed in Figure 8, with the increase of methane addition, the burning temperatures become lower in overall. It reinforces the findings in the study(Reuter et al., 2018), that the heat release from methane/DME cool flames is mainly controlled

by the low-temperature chemical processes of DME. Comparing Figures 8(a-c) with Figures 8(d-e), a notable distinction in their combustion modes can be recognized. With lower methane blending (R_m = 0-0.2), cool flames combust exclusively within the cool stable flame branches. When R_m rises to 30% and 40%, the fuel mixtures burn in both stable and unstable cool flame branches. This accords with the attached and lifted flame morphology displayed in Figure 6 and implies the occurrence of extinction/re-ignition events.

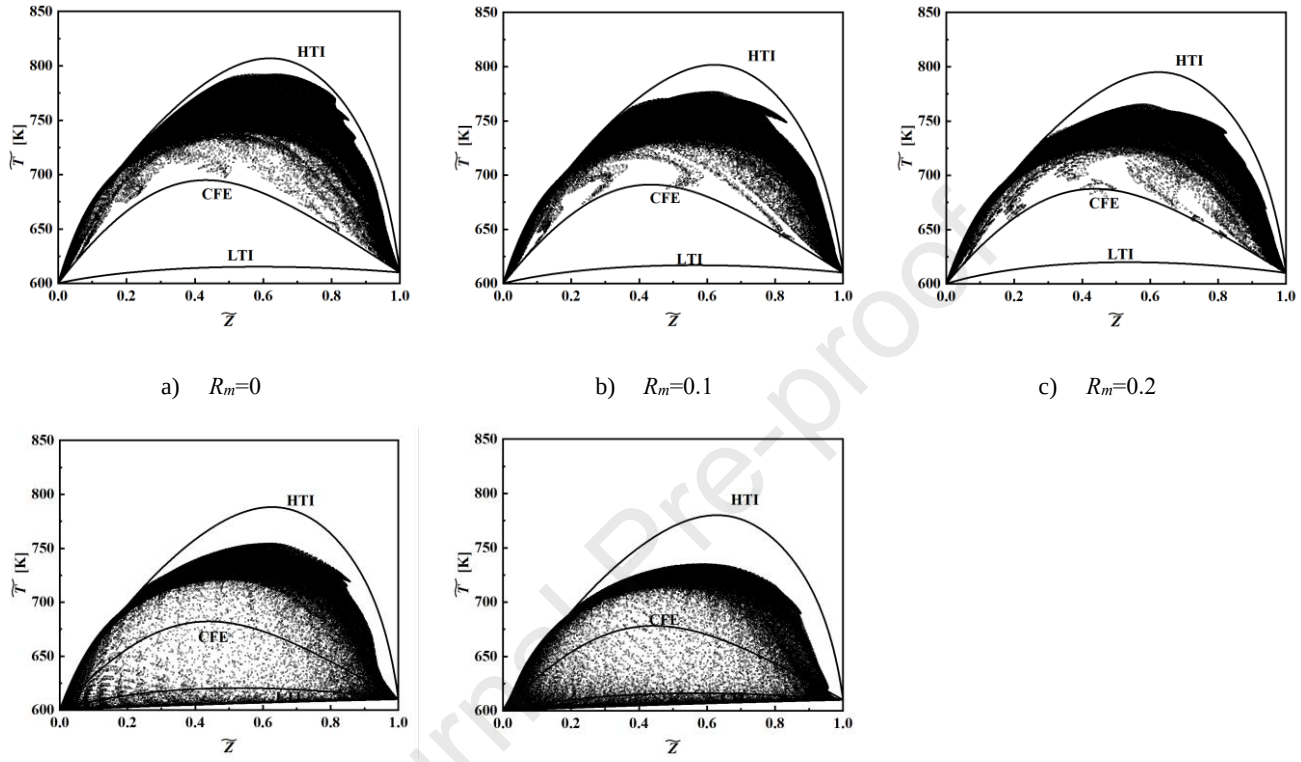

a) R_m=0 b) R_m=0.1 c) R_m=0.2

d) R_m=0.3 e) R_m=0.4

Figure 8 Instantaneous scatter plots of $\widetilde{T}$ as functions of $\widetilde{Z}$ under different R_m

To further analyze these unstable events, Figure 8d is divided into 3 segments according to the different flame structures in Figure 6d, specifically the inert mixing region, flame base region and flame brush region. The detailed distributions are expressed in Figure 9, along with the corresponding temperature contours. As shown in Figure 9a, all temperature scatters are exclusively confined to the unstable flame branches, indicating that the local thermochemical conditions in this region are essentially non-combusting or unable to maintain a stable diffusion flame structure. The highest recorded temperature of ~627 K (in contrast to the inlet temperature of 610 K) supplies critical evidence supporting the "inert" qualification: no significant chemical heat release, and then no active combustion. Such findings strongly confirm designating this upstream zone (0<x/D<2) as an "inert mixing region.

For Figure 9b, the binary mixtures burn in both stable and unstable cool flame branches, which is a hallmark

of the “flame base”. The simultaneous existence of stable and unstable branches suggests that active combustion is taking place, along with local extinctions and reignitions phenomena. Within this region, the competition between ignition (propagating upstream) and extinction/quenching (propagating downstream) processes occurs dynamically, and this autoignition stabilizes the cool flames.

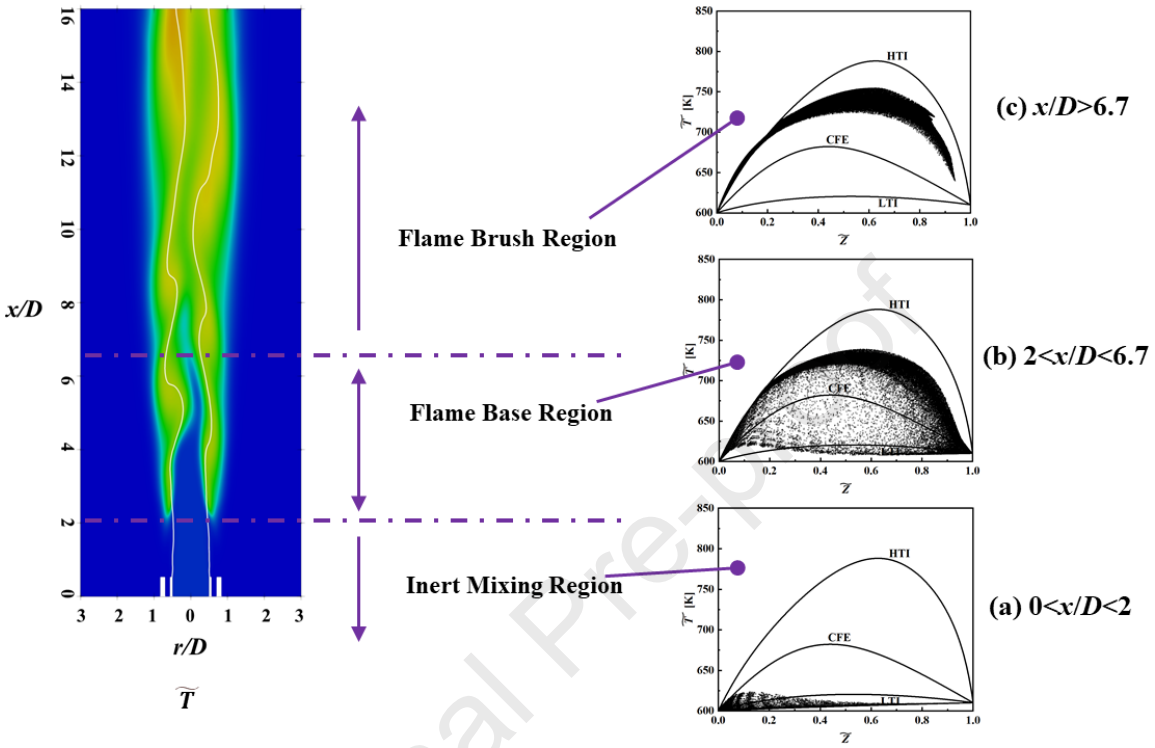

Figure 9 The instantaneous $\widetilde{T}$ scatters as functions of $\widetilde{Z}$ in different flame regions for R_m=0.3. The temperature contour is the same as Figure 6d.

Regarding the flame brush zone shown in Figure 9c, temperature points reside solely on the stable flame branch and a turbulent, brush-like flame spreads downstream of *x/D*=6.7, characteristic of large-scale vortices. This suggests that cool flame temperatures are sufficiently high, and low-temperature combustion is stably sustaining in the local turbulent atmosphere. These observations uncover the differing thermochemical characteristics across different flame structures for the methane/DME lifted turbulent cool flames.

4.3 Fuel consumption and product formation

To examine the impacts of methane addition on the low-temperature oxidation of fuel mixtures, the time-averaged DME and methane mass fraction fields in central longitudinal sections is presented in Figure 10, along with the white solid lines representing the iso-contours of the stoichiometric time-averaged mixture fraction. Meantime, the centerline distributions of the time-averaged DME, methane and their mole fraction ratios are shown

in Figure 11 for all the investigated fuel mixtures. As indicated by Figure 10 and 11, both the DME and methane keep an obviously descending trend along the centerline roughly after x/D=4. However, Figure 10c reveals a significant upward trend in their mole fraction ratios, demonstrating that the low-temperature oxidation rate of methane is lower than that of DME. Meanwhile, this upward trend also varies with different methane proportions: as the methane proportion increases, the slope of the upward curve (downstream of x/D=6) significantly rises. This evidences that the increase in methane addition inhibits the low-temperature oxidation rate of DME.

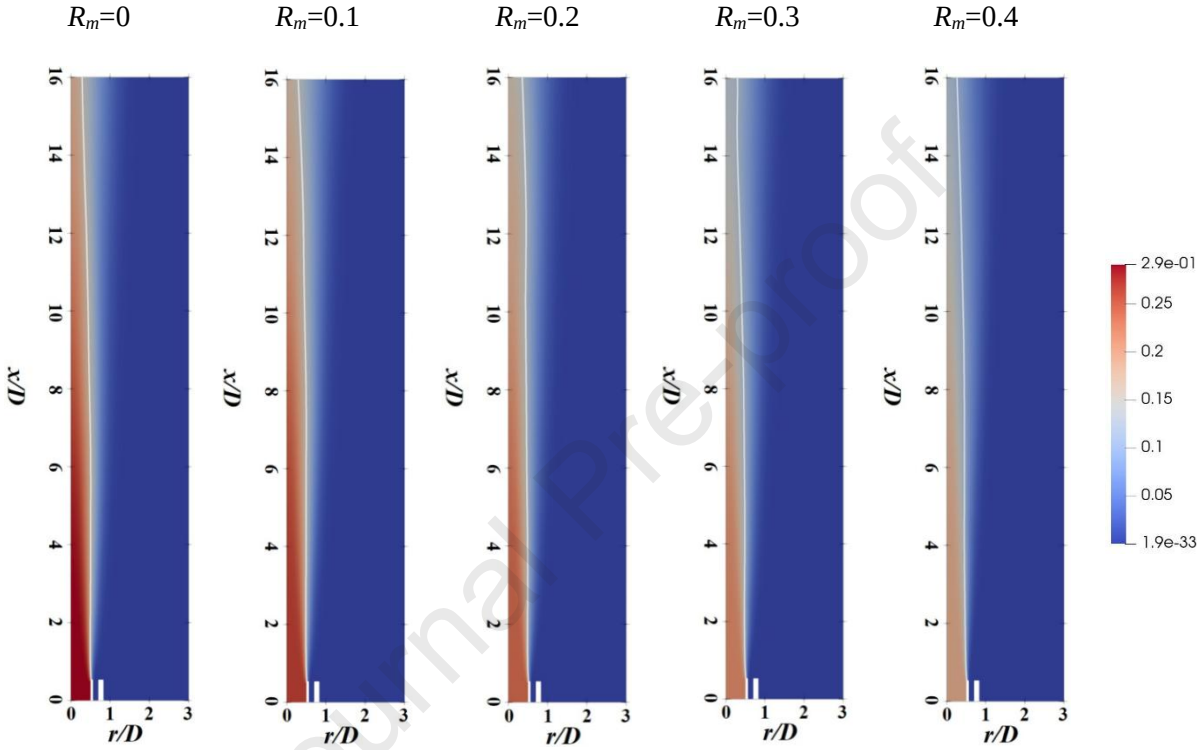

a) $\widetilde{\{DME\}}$

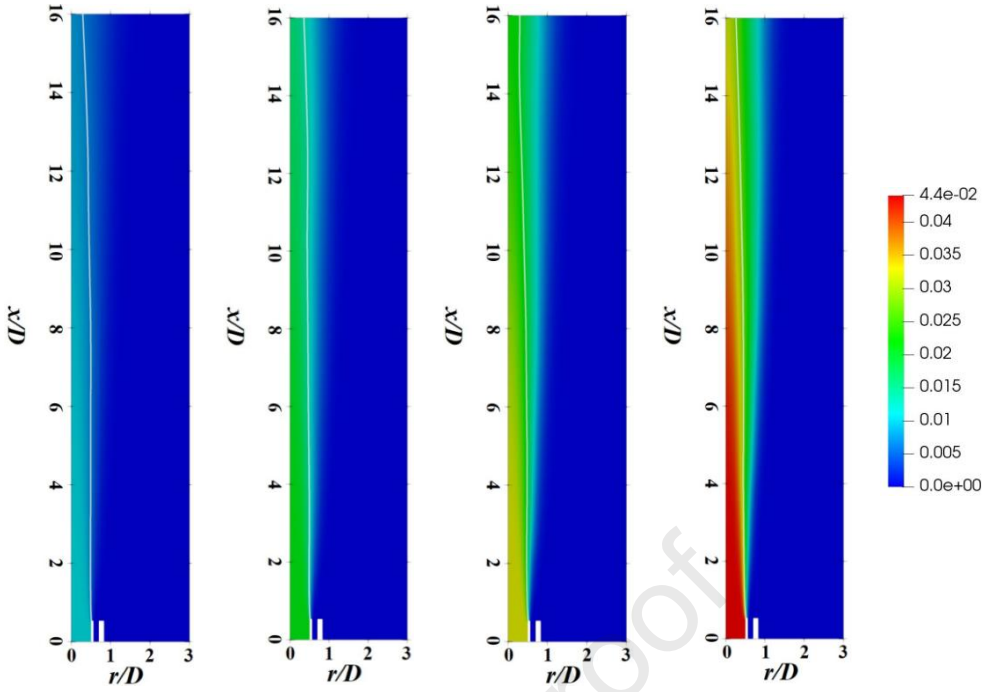

b) $\widetilde{\{CH_4\}}$

Figure 10 Time-averaged filtered mass fraction contours of reactants in central longitudinal sections

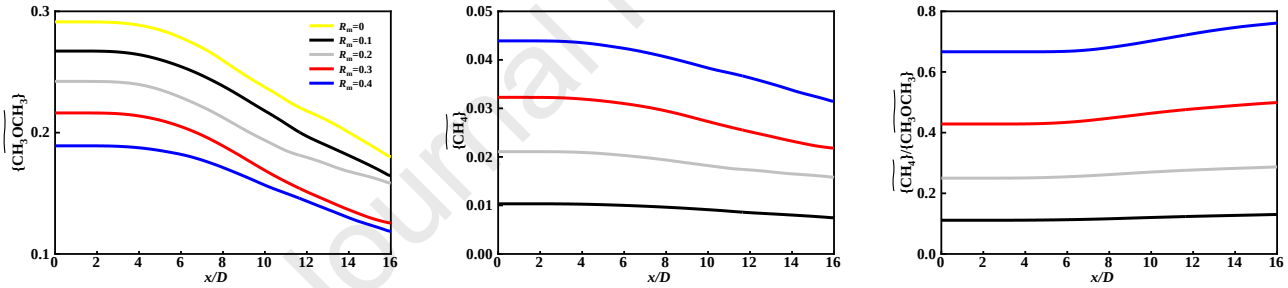

a) DME averaged mass fraction b) CH_4 averaged mass fraction c) Mole fraction ratios

Figure 11 The centerline distribution of the time-averaged DME, methane and their mole fraction ratios

To illustrate the kinetic interactions between methane and DME in cool flames, the chemical flux pathways of methane/DME cool flames at R_m =0/0.2/0.4 and χ_{st}= 60 s^{-1} is calculated by FlameMaster and is shown in Figure 12, along with the consumption proportions of OH in Table 2. As expressed in the figure, the major reaction flux pathways for DME/methane low-temperature oxidation can be briefly concluded as RH → R → RO_2 → QOOH → CH_2O (DME) and CH_4 → CH_3 → CH_3O_2 → CH_3O_2H → CH_3OH → CH_2OH →CH_2O (CH_4) respectively. Evidently, the H-abstraction reaction serves a vital function during the initial stages of both fuels' oxidation. According to Table 2, methane is in competition with DME for OH radicals through the reaction of

CH_4+OH<=>CH_3+H_2O, suppressing the H-abstraction reaction of DME. In spite, the cool flames of DME/methane mixtures are dominated by the oxidation of DME, as the consumption proportions of OH is less than that of DME by orders of magnitude even at R_m =0.4. Besides, the low-temperature oxidation of DME is dominated by "RH→ R→RO_2→QOOH" reactions. QOOH is the core intermediate, which either directly decomposes to produce CH_2O or go through the key reaction of O_2QOOH <=> HO_2CH_2OCHO + OH to generate CH_2O. The addition of methane would not alter the LTC pathways of DME, but would significantly inhibit the reaction of QOOH <=> O_2 + 2CH_2O. Although O_2QOOH <=> HO_2CH_2OCHO + OH is promoted at larger methane blending ratios, the reactions of OCH_2OCHO => $HOCH_2OCO$ is suppressed. These two mechanisms kinetically explain the different fuel consumption trends of methane and DME in Figures 10 and 11.

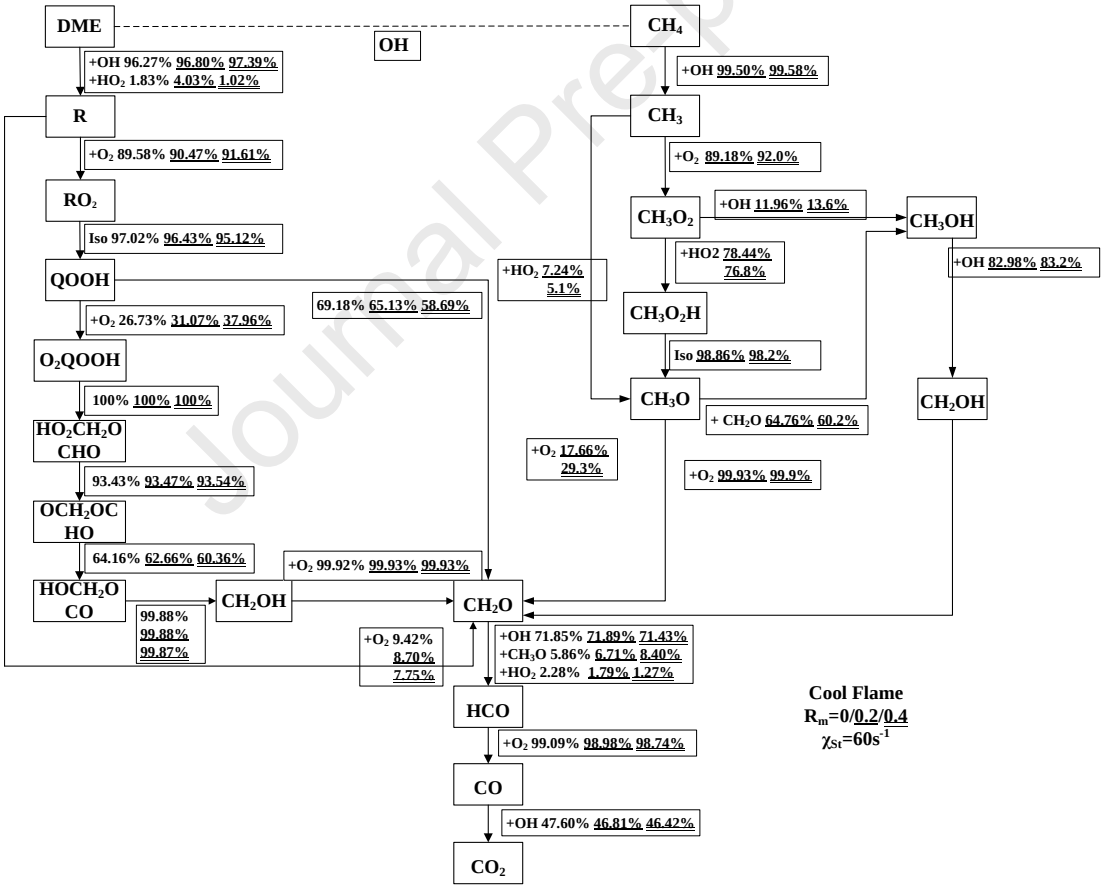

Figure 12 The chemical flux pathways of methane/DME cool flames at R_m =0/0.2/0.4 and χ_{st}= 60 s^{-1}. The other boundary conditions correspond to Table 1.

Table 2 The consumption proportions of OH at R_m =0/0.2/0.4 and χ_{st}= 60 s^{-1}

Reaction	Proportion				
	R_m =0	R_m =0.1	R_m =0.2	R_m =0.3	R_m =0.4
$CH_3OCH_3 + OH \rightarrow CH_3OCH_2 + H_2O$	81.21%	80.59%	79.92%	79.22%	78.54%
$CH_4 + OH \rightarrow CH_3 + H_2O$	/	0.42%	0.91%	1.53%	2.31%

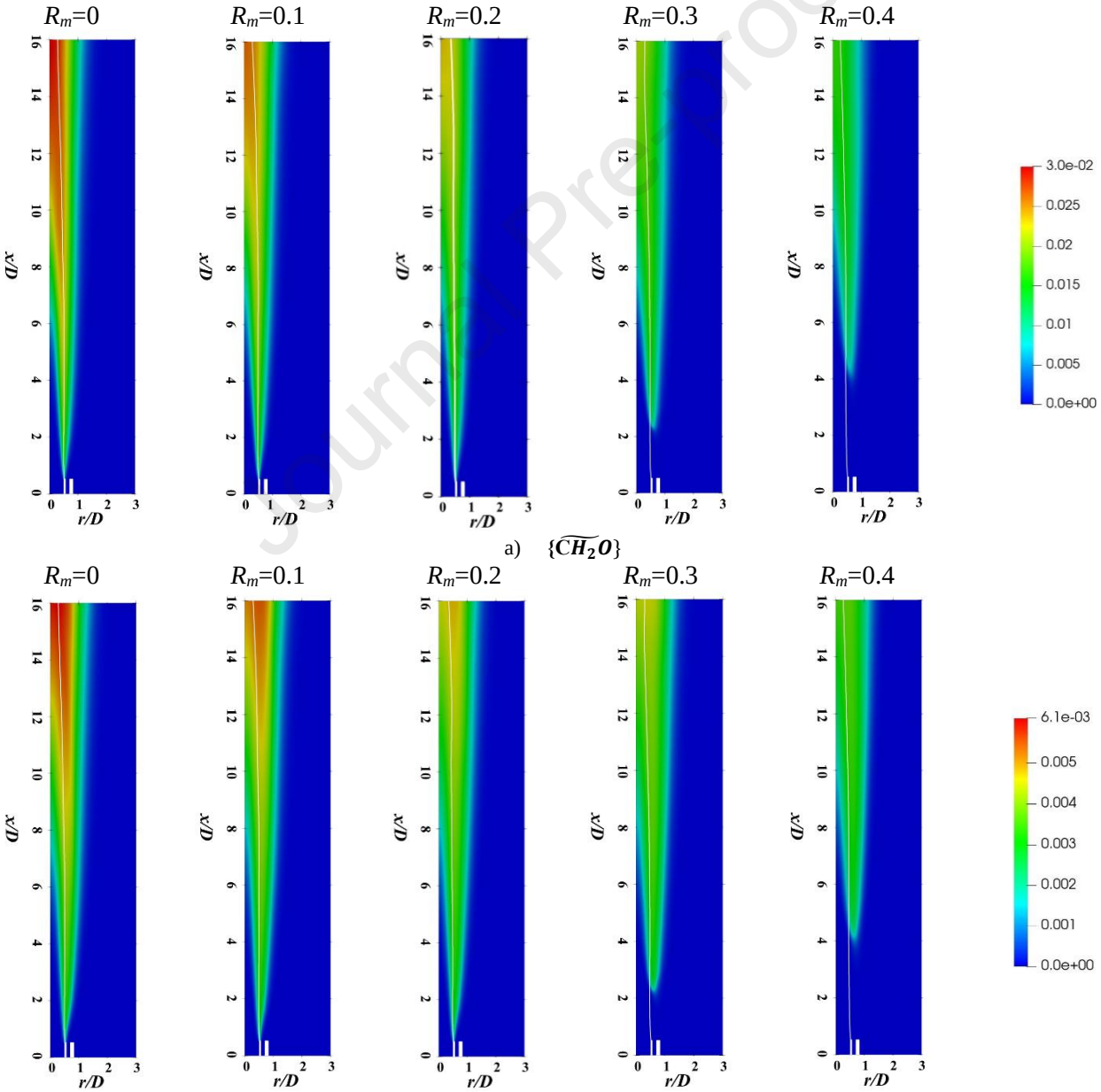

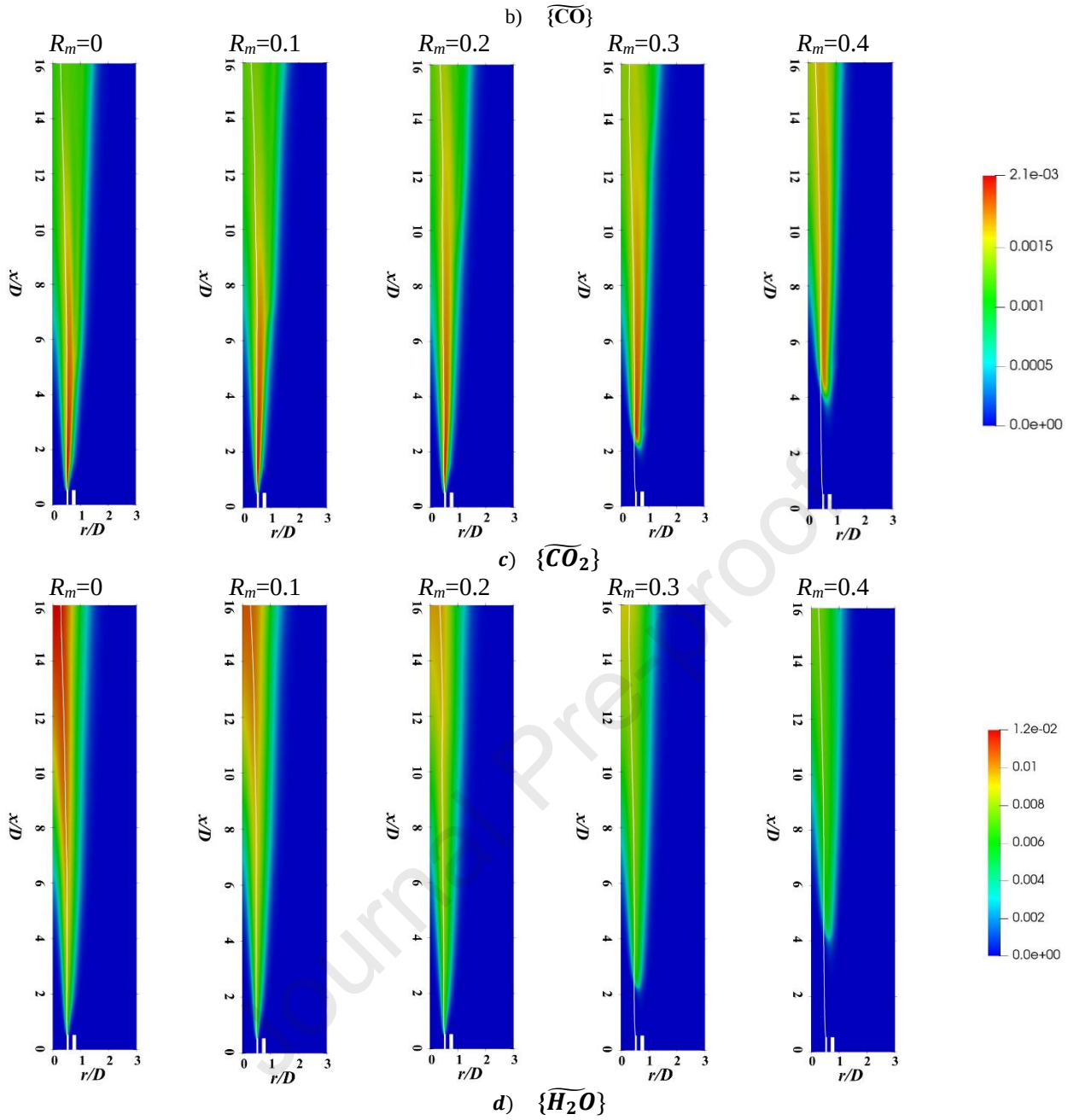

Figure 13 Time-averaged filtered mass fraction contours of key products in central longitudinal sections

As the key products of the DME/methane low-temperature oxidation, the time-averaged distribution of CH_2O, CO, CO_2 and H_2O are presented in Figure 13. As can be seen, the distribution of CO_2 is different from that of the other 3 species in the streamwise direction: CO_2 accumulates in the upstream near the fuel nozzle and exhibit a declining trend downstream, while the trend is opposite for CH_2O, CO, and H_2O. On the other hand, the overall amount of all these four species is decreasing in response to the increase of methane blending ratios. By analyzing the reaction flux pathway in Figure 12, the formation of CH_2O stem from two oxidation reaction pathways of DME and CH_4. However, according to Table 2, the OH consumption proportion by DME oxidation is far larger than that

of CH_4 oxidation, indicating that the low-temperature reactivity of methane is extremely low. Thus, the formation of CH_2O is decisively determined by the reaction pathway of DME low-temperature oxidation. As explained in Figure 12, the addition of methane would significantly inhibit the reaction of QOOH <=> O_2 + 2CH_2O, a vital step in oxidation reaction pathways of DME. This kinetically explains why the formation of CH_2O decrease with the increase of methane blending ratios. Furthermore, the formation of CO and CO_2 are directly related to CH_2O, as suggested by the reaction flux pathway. The drop of CH_2O yielding leads to the decrease of CO and CO_2, when the methane proportions decline.

4.4 Correlation between temperatures and key intermediate formation

In terms of cool flames, it is noteworthy to investigate the correlation between key intermediate formation and temperature distribution. Figure 14 displays scatter plots of time-averaged mass fractions of CH_2O, CO, CO_2 and H_2O as functions of $\{\widetilde{T}\}$ for different methane blending ratios and their linear-fitted lines. It is evident that the distributions of CH_2O, CO, and H_2O show a strong positive linear correlation with temperature across different methane blending ratios, as the coefficients of determination in linear fits, R^2, are all greater than 95%. Besides, the correlation between *T* and the distributions of CO and H_2O is not sensitive to the methane blending ratios, since the slope of their linear-fitted lines is close. As to CO_2, it shows a weaker positive linear correlation with temperature at R_m=0 and 0.1 (R^2<95%) until the correlation becomes strong at larger methane blending ratios (R^2>95%). On the other hand, the correlation between *T* and the distributions of CH_2O and CO_2 is sensitive to the methane blending ratios, since the slope of their linear-fitted lines is obviously differentiated by methane addition.

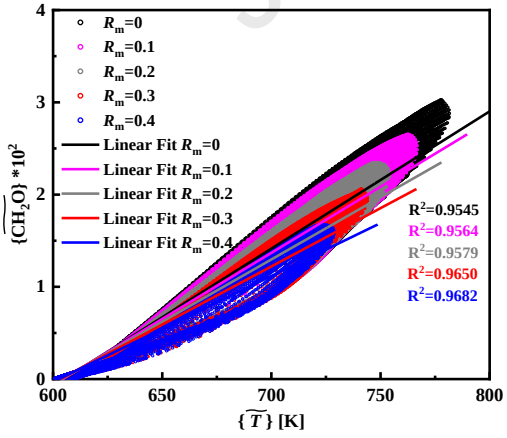

(a) CH_2O

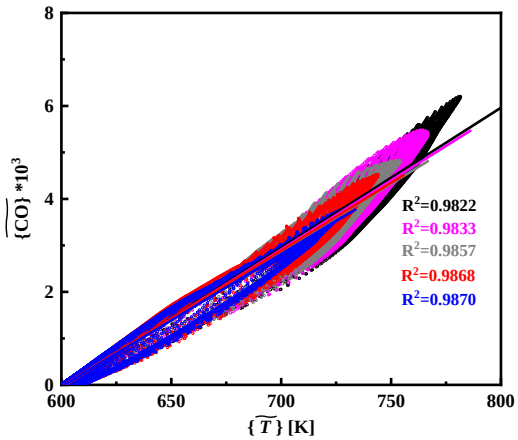

(b) CO

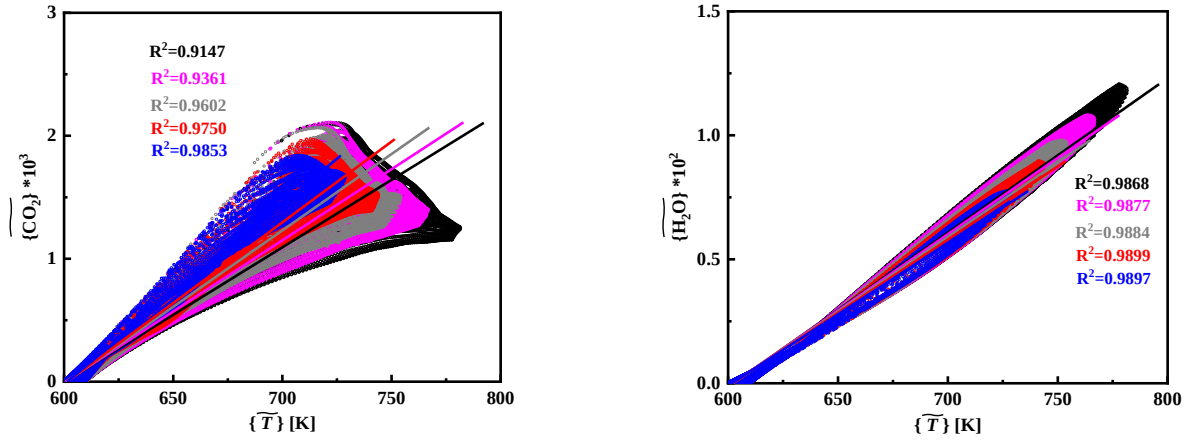

(c) CO_2 (d) H_2O

Figure 14 Scatter plots of time-averaged mass fractions of CH_2O, CO, CO_2 and H_2O as functions of $\{\widetilde{T}\}$ for different methane blending ratios

5. Conclusion

In present work, the turbulent non-premixed cool flames of dimethyl-ether (DME)/methane mixtures are studied within the framework of flamelet/progress variable modelling and chemical kinetic analyses. The numerical setup is based on the Princeton CARAT burner configuration, and the accuracy of the hpmech-V3.3 chemistry to model turbulent low-temperature combustion is validated against the referenced experiments and DNS. The findings are summarized as follows:

The FPV-LES results demonstrate that the turbulent cool flame structures are influenced by methane addition through the change of cool flame extinction limits and become lifted with the increase of methane blending ratios. The different flame regions associated with differing thermochemical characteristics for the lifted cool flames are revealed as inert mixing region (sparsely unstable cool flame branch), flame base region (coexistence of stable and unstable cool flame branches), and flame brush region (predominantly stable cool flame branch).

The DME/methane consumption trends suggest that methane addition inhibits the DME low-temperature oxidation. Through the kinetic analyses, the mechanisms are identified to be two-fold: methane competes with the DME H-abstraction reaction for OH radicals and the reaction of QOOH <=> O_2 + 2CH_2O is significantly slowed down with the methane addition. The mechanisms also kinetically explain the finding that the formation of CH_2O, CO, CO_2 in cool flames decline in response to the increase of methane blending ratios.

The distributions of CH_2O, CO, CO_2 and H_2O show a positive linear correlation with temperature. While the correlation between T and the distributions of CH_2O and CO_2 is sensitive to the methane blending ratios, that

between T and the distributions of CO and H_2O is not.

Acknowledgements

This work is financially supported by Taishan Scholars Youth Expert Program of Shandong Province (tsqn202507006), Natural Science Foundation of Shandong Province (ZR2021QE144), Key Research and Development Program of Shandong Province (2022CXPT034) and Sichuan Provincial College Students Innovation Training Program (S202511079060), and the Talent Program of Chengdu University (Z3390).

References

Ajayi-Banji, A.A., Rahman, S., 2024. Impact of agitation and non-agitation on microbiota and reactor performance in anaerobic digestion. Green Energy Resour. 2, 100056. https://doi.org/10.1016/j.gerr.2024.100056

Amann, M., Alger, T., Mehta, D., 2011. The Effect of EGR on Low-Speed Pre-Ignition in Boosted SI Engines. SAE Int. J. Engines 4, 235–245. https://doi.org/10.4271/2011-01-0339

Banke, K., Hegner, R., Schröder, D., Schulz, C., Atakan, B., Kaiser, S.A., 2019. Power and syngas production from partial oxidation of fuel-rich methane/DME mixtures in an HCCI engine. Fuel 243, 97–103. https://doi.org/10.1016/j.fuel.2019.01.076

Benteux, L., Hu, X., Liang, W., Law, C.K., Valiev, D.M., 2025. Steady hot and cool dimethyl ether premixed flames in channels with wall heat loss. Combust. Flame 274, 113982. https://doi.org/10.1016/j.combustflame.2025.113982

Bilger, R.W., 1989. Turbulent Diffusion Flames. Annu. Rev. Fluid Mech. 21, 101–135. https://doi.org/10.1146/annurev.fl.21.010189.000533

Bradley, D., Kalghatgi, G.T., 2009. Influence of autoignition delay time characteristics of different fuels on pressure waves and knock in reciprocating engines. Combust. Flame 156, 2307–2318. https://doi.org/10.1016/j.combustflame.2009.08.003

Burke, U., Somers, K.P., O'Toole, P., Zinner, C.M., Marquet, N., Bourque, G., Petersen, E.L., Metcalfe, W.K., Serinyel, Z., Curran, H.J., 2015. An ignition delay and kinetic modeling study of methane, dimethyl ether, and their mixtures at high pressures. Combust. Flame 162, 315–330. https://doi.org/10.1016/j.combustflame.2014.08.014

Chai, X., Tonjes, D.J., Mahajan, D., 2016. Methane emissions as energy reservoir: Context, scope, causes and mitigation strategies. Prog. Energy Combust. Sci. 56, 33–70. https://doi.org/10.1016/j.pecs.2016.05.001

Chen, Z.X., Langella, I., Barlow, R.S., Swaminathan, N., 2020. Prediction of local extinctions in piloted jet flames with inhomogeneous inlets using unstrained flamelets. Combust. Flame 212, 415–432. https://doi.org/10.1016/j.combustflame.2019.11.007

Dbouk, Z., Benoit, R., Hoblos, B., Belhadj, N., Dagaut, P., 2025. Cool flame of methylcyclohexene isomers in a JSR: Formation of aromatic and polyunsaturated hydrocarbons. Fuel 381, 133644. https://doi.org/10.1016/j.fuel.2024.133644

Deng, S., Zhao, P., Zhu, D., Law, C.K., 2014. NTC-affected ignition and low-temperature flames in nonpremixed DME/air counterflow. Combust. Flame 161, 1993–1997. https://doi.org/10.1016/j.combustflame.2014.01.020

Desai, S., Sankaran, R., Im, H.G., 2020. Auto-ignitive deflagration speed of methane (CH4) blended dimethyl-ether (DME)/air mixtures at stratified conditions. Combust. Flame 211, 377–391. https://doi.org/10.1016/j.combustflame.2019.10.001

Ezoji, H., Shafaghat, R., Jahanian, O., 2019. Numerical simulation of dimethyl ether/natural gas blend fuel HCCI combustion to investigate the effects of operational parameters on combustion and emissions. J. Therm. Anal. Calorim. 135, 1775–1785. https://doi.org/10.1007/s10973-018-7271-2

Gaipl, L., Jaravel, T., Douasbin, Q., Poinsot, T., 2025. LES of the combustion efficiency of wake stabilized methane jet flames in crossflow. Combust. Flame 273, 113916. https://doi.org/10.1016/j.combustflame.2024.113916

Gao, Z., Wang, H., Song, C., Luo, K., Fan, J., 2020. Large-eddy simulation of hydrothermal flames using extended flamelet/progress variable approach. J. Supercrit. Fluids 163, 104843. https://doi.org/10.1016/j.supflu.2020.104843

Ge, J.C., Luo, H., Im, I.-T., Choi, N.J., 2025a. Comprehensive analysis of the preparation of waste frying oil biodiesel and its application characteristics in diesel engines based on recycling economic structure in South Korea. Energy 330, 136949. https://doi.org/10.1016/j.energy.2025.136949

Ge, J.C., Luo, H., Im, I.-T., Choi, N.J., 2025b. Combustion and emission benefits of ultrasound-processed biodiesel-gasoline-ethanol blends in compression ignition engines. Case Stud. Therm. Eng. 75, 107076. https://doi.org/10.1016/j.csite.2025.107076

Gicquel, L.Y.M., Staffelbach, G., Poinsot, T., 2012. Large Eddy Simulations of gaseous flames in gas turbine combustion chambers. Prog. Energy Combust. Sci. 38, 782–817. https://doi.org/10.1016/j.pecs.2012.04.004

Guo, S., Wang, J., Wei, X., Yu, S., Zhang, M., Huang, Z., 2018. Numerical simulation of premixed combustion using the modified dynamic thickened flame model coupled with multi-step reaction mechanism. Fuel 233, 346–353. https://doi.org/10.1016/j.fuel.2018.06.074

Hashemi, H., Christensen, J.M., Glarborg, P., 2019. High-pressure pyrolysis and oxidation of DME and DME/CH4. Combust. Flame 205, 80–92. https://doi.org/10.1016/j.combustflame.2019.03.028

Hegner, R., Werler, M., Schießl, R., Maas, U., Atakan, B., 2017. Fuel-Rich HCCI Engines as Chemical Reactors for Polygeneration: A Modeling and Experimental Study on Product Species and Thermodynamics. Energy Fuels 31, 14079–14088. https://doi.org/10.1021/acs.energyfuels.7b02150

H.Pitsch, n.d. FlameMaster: A C++ computer program for 0D combustion and 1D laminar flame calculations. 1998.

Ihme, M., Cha, C.M., Pitsch, H., 2005. Prediction of local extinction and re-ignition effects in non-premixed turbulent combustion using a flamelet/progress variable approach. Proc. Combust. Inst. 30, 793–800. https://doi.org/10.1016/j.proci.2004.08.260

Ihme, M., Pitsch, H., 2008a. Prediction of extinction and reignition in nonpremixed turbulent flames using a flamelet/progress variable model: 2. Application in LES of Sandia flames D and E. Combust. Flame 155, 90–107. https://doi.org/10.1016/j.combustflame.2008.04.015

Ihme, M., Pitsch, H., 2008b. Prediction of extinction and reignition in nonpremixed turbulent flames using a flamelet/progress variable model: 1. A priori study and presumed PDF closure. Combust. Flame 155, 70–89. https://doi.org/10.1016/j.combustflame.2008.04.001

Ihme, M., Shunn, L., Zhang, J., 2012a. Regularization of reaction progress variable for application to flamelet-based combustion models. J. Comput. Phys. 231, 7715–7721. https://doi.org/10.1016/j.jcp.2012.06.029

Ihme, M., Shunn, L., Zhang, J., 2012b. Regularization of reaction progress variable for application to flamelet-based combustion models. J. Comput. Phys. 231, 7715–7721. https://doi.org/10.1016/j.jcp.2012.06.029

Jiang, X., Mira, D., Cluff, D.L., 2018. The combustion mitigation of methane as a non-CO2 greenhouse gas. Prog. Energy Combust. Sci. 66, 176–199. https://doi.org/10.1016/j.pecs.2016.06.002

Jin, T., Wu, Y., Wang, X., Luo, K.H., Lu, T., Luo, K., Fan, J., 2019. Ignition dynamics of DME/methane-air reactive mixing layer under reactivity controlled compression ignition conditions: Effects of cool flames. Appl. Energy 249, 343–354. https://doi.org/10.1016/j.apenergy.2019.04.161

Ju, Y., 2021. Understanding cool flames and warm flames. Proc. Combust. Inst. 38, 83–119. https://doi.org/10.1016/j.proci.2020.09.019

Ju, Y., Reuter, C.B., Yehia, O.R., Farouk, T.I., Won, S.H., 2019. Dynamics of cool flames. Prog. Energy Combust. Sci. 75, 100787. https://doi.org/10.1016/j.pecs.2019.100787

Kaczmarek, D., Herzler, J., Porras, S., Shaqiri, S., Fikri, M., Schulz, C., Atakan, B., Maas, U., Kasper, T., 2021. Plug-flow reactor and shock-tube study of the oxidation of very fuel-rich natural gas/DME/O2 mixtures. Combust. Flame 225, 86–103. https://doi.org/10.1016/j.combustflame.2020.10.004

Kim, W.-W., Menon, S., 1995. A new dynamic one-equation subgrid-scale model for large eddy simulations, in: 33rd Aerospace Sciences Meeting and Exhibit, Aerospace Sciences Meetings. American Institute of Aeronautics and Astronautics. https://doi.org/10.2514/6.1995-356

Kokjohn, S., Hanson, R., Splitter, D., Kaddatz, J., Reitz, R., 2011. Fuel Reactivity Controlled Compression Ignition (RCCI) Combustion in Light- and Heavy-Duty Engines. SAE Int. J. Engines 4, 360–374.

Kornev, N., Hassel, E., n.d. Method of random spots for generation of synthetic inhomogeneous turbulent fields with prescribed autocorrelation functions. https://doi.org/10.1002/cnm.880

Li, J., Tang, A., Cai, T., Zhou, C., 2020. Effect of dimethyl ether addition on flame stability of premixed methane/air in a micro-planar quartz combustor. Chem. Eng. Process. - Process Intensif. 147, 107740. https://doi.org/10.1016/j.cep.2019.107740

Li, N., Bykov, V., Moroshkina, A., Sereshchenko, E., Gubernov, V., 2025. Two dimensional flame structure of oscillating burner-stabilized methane-air flames. Combust. Flame 276, 114115.

https://doi.org/10.1016/j.combustflame.2025.114115
Liang, W., Law, C.K., 2017. Extended flammability limits of *n*-heptane/air mixtures with cool flames. Combust. Flame 185, 75–81. https://doi.org/10.1016/j.combustflame.2017.06.015
Lowry, W.B., Serinyel, Z., Krejci, M.C., Curran, H.J., Bourque, G., Petersen, E.L., 2011. Effect of methane-dimethyl ether fuel blends on flame stability, laminar flame speed, and Markstein length. Proc. Combust. Inst. 33, 929–937. https://doi.org/10.1016/j.proci.2010.05.042
Lu, M., Fu, Z., Yuan, X., Sun, G., Jia, G., 2021. Study of the reduced kinetic mechanism of methane/dimethyl ether combustion. Fuel 303, 121308. https://doi.org/10.1016/j.fuel.2021.121308
Lu, M., Wan, K., Zhu, X., He, Y., Zhu, Y., Yuan, Y., Cai, Q., Gao, Z., Jiang, C., 2024. Investigation of swirl premixed dimethyl ether/methane flame stability and combustion characteristics in an industrial gas turbine combustor. Energy 310, 133255. https://doi.org/10.1016/j.energy.2024.133255
Luo, H., Yu, M., Zhai, C., An, Y., Wang, C., Nishida, K., 2023. Study on fermentation gas combustion with hydrogen addition under various throttle openings. Green Energy Resour. 1, 100003. https://doi.org/10.1016/j.gerr.2022.100003
Luo, J., Li, W., Tian, L., Liu, L., 2017. Experimental and Numerical Study of Oxygen Diluted Partially Premixed Dimethyl Ether/ Methane Counter Flow Flame. Chem. Eng. Trans. 61, 415–420. https://doi.org/10.3303/CET1761067
Mohammad, A., Juhany, K.A., 2019. Laminar burning velocity and flame structure of DME/methane + air mixtures at elevated temperatures. Fuel 245, 105–114. https://doi.org/10.1016/j.fuel.2019.02.085
Moroshkina, A., Babina, S., Ponomareva, A., Sereshchenko, E., Mislavskii, V., Gubernov, V., Bykov, V., 2025. Numerical and experimental study of stability limits of methane-air flame stabilized on a flat porous burner at normal and elevated pressure. Combust. Flame 280, 114336. https://doi.org/10.1016/j.combustflame.2025.114336
Murakami, Y., Reuter, C.B., Yehia, O.R., Ju, Y., 2021. Studies of autoignition-assisted nonpremixed cool flames. Proc. Combust. Inst. 38, 2333–2340. https://doi.org/10.1016/j.proci.2020.06.379
Nakamura, H., Sugita, T., Tezuka, T., Maruta, K., 2021. Study on methane oxidation affected by dimethyl ether oxidation at low temperatures using a micro flow reactor with a controlled temperature profile. Combust. Flame 223, 320–329. https://doi.org/10.1016/j.combustflame.2020.10.006
Nakyai, T., Saebea, D., 2019. Exergoeconomic comparison of syngas production from biomass, coal, and natural gas for dimethyl ether synthesis in single-step and two-step processes. J. Clean. Prod. 241, 118334. https://doi.org/10.1016/j.jclepro.2019.118334
Novoselov, A.G., Law, C.K., Mueller, M.E., 2019a. Direct Numerical Simulation of turbulent nonpremixed "cool" flames: Applicability of flamelet models. Proc. Combust. Inst. 37, 2143–2150. https://doi.org/10.1016/j.proci.2018.06.191
Novoselov, A.G., Reuter, C.B., Yehia, O.R., Won, S.H., Fu, M.K., Kokmanian, K., Hultmark, M., Ju, Y., Mueller, M.E., 2019b. Turbulent nonpremixed cool flames: Experimental measurements, Direct Numerical Simulation, and manifold-based combustion modeling. Combust. Flame 209, 144–154. https://doi.org/10.1016/j.combustflame.2019.07.034
OIJEN, J.A.V., GOEY, L.P.H.D., 2000. Modelling of Premixed Laminar Flames using Flamelet-Generated Manifolds. Combust. Sci. Technol. https://doi.org/10.1080/00102200008935814
Pant, T., Han, C., Wang, H., 2019. Examination of errors of table integration in flamelet/progress variable modeling of a turbulent non-premixed jet flame. Appl. Math. Model. 72, 369–384. https://doi.org/10.1016/j.apm.2019.03.016
Park, S.H., Lee, C.S., 2013. Combustion performance and emission reduction characteristics of automotive DME engine system. Prog. Energy Combust. Sci. 39, 147–168. https://doi.org/10.1016/j.pecs.2012.10.002
Peters, N., 1988. Laminar flamelet concepts in turbulent combustion. Symp. Int. Combust., Twenty-First Symposuim (International on Combustion) 21, 1231–1250. https://doi.org/10.1016/S0082-0784(88)80355-2
Pierce, C.D., Moin, P., 2004. Progress-variable approach for large-eddy simulation of non-premixed turbulent combustion. J. Fluid Mech. 504, 73–97. https://doi.org/10.1017/S0022112004008213
Porras, S., Kaczmarek, D., Herzler, J., Drost, S., Werler, M., Kasper, T., Fikri, M., Schießl, R., Atakan, B., Schulz, C., Maas, U., 2020. An experimental and modeling study on the reactivity of extremely fuel-rich methane/dimethyl ether mixtures. Combust. Flame 212, 107–122. https://doi.org/10.1016/j.combustflame.2019.09.036
Qi, C., Dai, P., Yu, H., Chen, Z., 2017. Different modes of reaction front propagation in *n*-heptane/air mixture with concentration non-uniformity. Proc. Combust. Inst. 36, 3633–3641.

https://doi.org/10.1016/j.proci.2016.06.086
Reuter, C.B., Lee, M., Won, S.H., Ju, Y., 2017. Study of the low-temperature reactivity of large *n*-alkanes through cool diffusion flame extinction. Combust. Flame 179, 23–32. https://doi.org/10.1016/j.combustflame.2017.01.028
Reuter, C.B., Won, S.H., Ju, Y., 2016. Experimental study of the dynamics and structure of self-sustaining premixed cool flames using a counterflow burner. Combust. Flame 166, 125–132. https://doi.org/10.1016/j.combustflame.2016.01.008
Reuter, C.B., Zhang, R., Yehia, O.R., Rezgui, Y., Ju, Y., 2018. Counterflow flame experiments and chemical kinetic modeling of dimethyl ether/methane mixtures. Combust. Flame 196, 1–10. https://doi.org/10.1016/j.combustflame.2018.06.004
See, Y.C., Ihme, M., 2015. Large eddy simulation of a partially-premixed gas turbine model combustor. Proc. Combust. Inst. 35, 1225–1234. https://doi.org/10.1016/j.proci.2014.08.006
Sen, F., Shu, B., Kasper, T., Herzler, J., Welz, O., Fikri, M., Atakan, B., Schulz, C., 2016. Shock-tube and plug-flow reactor study of the oxidation of fuel-rich CH4/O2 mixtures enhanced with additives. Combust. Flame 169, 307–320. https://doi.org/10.1016/j.combustflame.2016.03.030
Smagorinsky, J., 1963. GENERAL CIRCULATION EXPERIMENTS WITH THE PRIMITIVE EQUATIONS.
Sun, W., Won, S.H., Gou, X., Ju, Y., 2015. Multi-scale modeling of dynamics and ignition to flame transitions of high pressure stratified *n*-heptane/toluene mixtures. Proc. Combust. Inst. 35, 1049–1056. https://doi.org/10.1016/j.proci.2014.05.141
Tang, J., Kang, L., Liu, Y., 2023. Demand oriented planning of methanol-dimethyl ether co-production system for CO2 reduction. J. Clean. Prod. 421, 138520. https://doi.org/10.1016/j.jclepro.2023.138520
Uddin, M.M., Simson, A., Wright, M.M., 2020. Techno-economic and greenhouse gas emission analysis of dimethyl ether production via the bi-reforming pathway for transportation fuel. Energy 211, 119031. https://doi.org/10.1016/j.energy.2020.119031
van Oijen, J.A., Donini, A., Bastiaans, R.J.M., ten Thije Boonkkamp, J.H.M., de Goey, L.P.H., 2016. State-of-the-art in premixed combustion modeling using flamelet generated manifolds. Prog. Energy Combust. Sci. 57, 30–74. https://doi.org/10.1016/j.pecs.2016.07.001
Wan, S., Fan, Y., Maruta, K., Suzuki, Y., 2019. Wall chemical effect of metal surfaces on DME/air cool flame in a micro flow reactor. Proc. Combust. Inst. 37, 5655–5662. https://doi.org/10.1016/j.proci.2018.05.165
Wang, L., Qi, Y., Yang, Z., Wu, H., Liu, J., Tang, Y., Wang, F., 2023. Pt nanoparticles supported LaCoO3 as highly efficient catalysts for photo-thermal catalytic CO2 methanation. Green Energy Resour. 1, 100036. https://doi.org/10.1016/j.gerr.2023.100036
Wang, Z., Gou, X., 2019. Cool flame characteristics of methane/oxygen mixtures. J. Energy Inst. 92, 2004–2010. https://doi.org/10.1016/j.joei.2018.10.011
Wang, Z., Wang, S., Whiddon, R., Han, X., He, Y., Cen, K., 2018. Effect of hydrogen addition on laminar burning velocity of CH4/DME mixtures by heat flux method and kinetic modeling. Fuel 232, 729–742. https://doi.org/10.1016/j.fuel.2018.05.146
Wang, Z., Yan, C., Lin, Y., Zhou, M., Jiang, B., Liu, N., Zhong, H., Ju, Y., 2023. Kinetics and extinction of non-premixed cool and warm flames of dimethyl ether at elevated pressure. Proc. Combust. Inst. 39, 1871–1879. https://doi.org/10.1016/j.proci.2022.06.007
Wang, Z., Zhang, X., Xing, L., Zhang, L., Herrmann, F., Moshammer, K., Qi, F., Kohse-Höinghaus, K., 2015. Experimental and kinetic modeling study of the low- and intermediate-temperature oxidation of dimethyl ether. Combust. Flame 162, 1113–1125. https://doi.org/10.1016/j.combustflame.2014.10.003
Weller, H.G., Tabor, G., Jasak, H., Fureby, C., 1998. A tensorial approach to computational continuum mechanics using object-oriented techniques. Comput. Phys. 12, 620–631. https://doi.org/10.1063/1.168744
Wu, X., 2017. Inflow Turbulence Generation Methods. Annu. Rev. Fluid Mech. 49, 23–49. https://doi.org/10.1146/annurev-fluid-010816-060322
Xiong, G., Li, G., Zeng, W., Liang, J., 2023. Flamelet LES of a turbulent non-premixed cool flame. Fuel 342, 127670. https://doi.org/10.1016/j.fuel.2023.127670
Xu, S., Li, G., Zhou, M., Yu, W., Zhang, Z., Hou, D., Yu, F., 2022. Experimental and kinetic studies of extinction limits of counterflow cool and hot diffusion flames of ammonia/*n*-dodecane. Combust. Flame 245, 112316. https://doi.org/10.1016/j.combustflame.2022.112316
Yan, C., Zhao, H., Wang, Z., Song, G., Lin, Y., Mulvihill, C.R., Jasper, A.W., Klippenstein, S.J., Ju, Y., 2022a. Low- and intermediate-temperature oxidation of dimethyl ether up to 100 atm in a supercritical pressure jet-stirred reactor. Combust. Flame, A dedication to Professor Katharina Kohse-Höinghaus 243, 112059. https://doi.org/10.1016/j.combustflame.2022.112059

Yan, C., Zhao, H., Wang, Z., Song, G., Lin, Y., Mulvihill, C.R., Jasper, A.W., Klippenstein, S.J., Ju, Y., 2022b. Low- and intermediate-temperature oxidation of dimethyl ether up to 100 atm in a supercritical pressure jet-stirred reactor. Combust. Flame, A dedication to Professor Katharina Kohse-Höinghaus 243, 112059. https://doi.org/10.1016/j.combustflame.2022.112059

Yao, M., Zheng, Z., Liu, H., 2009. Progress and recent trends in homogeneous charge compression ignition (HCCI) engines. Prog. Energy Combust. Sci. 35, 398–437. https://doi.org/10.1016/j.pecs.2009.05.001

Yu, H., Hu, E., Cheng, Y., Zhang, X., Huang, Z., 2014. Experimental and numerical study of laminar premixed dimethyl ether/methane–air flame. Fuel 136, 37–45. https://doi.org/10.1016/j.fuel.2014.07.032

Zeng, W., Zhou, F., Wang, X., Liang, J., 2026. FPV-LES of turbulent non-premixed ammonia/*n*-dodecane cool flames: effects of ammonia blending ratios. Fuel 406, 136950. https://doi.org/10.1016/j.fuel.2025.136950

Zhang, H., Kaczmarek, D., Rudolph, C., Schmitt, S., Gaiser, N., Oßwald, P., Bierkandt, T., Kasper, T., Atakan, B., Kohse-Höinghaus, K., 2022. Dimethyl ether (DME) and dimethoxymethane (DMM) as reaction enhancers for methane: Combining flame experiments with model-assisted exploration of a polygeneration process. Combust. Flame 237, 111863. https://doi.org/10.1016/j.combustflame.2021.111863

Zhang, M., Mao, R., Li, H., An, Z., Chen, Z.X., 2024. Graphics processing unit/artificial neural network-accelerated large-eddy simulation of swirling premixed flames. Phys. Fluids 36, 055147. https://doi.org/10.1063/5.0202321

Zhang, T., Ju, Y., 2020. Structures and propagation speeds of autoignition-assisted premixed *n*-heptane/air cool and warm flames at elevated temperatures and pressures. Combust. Flame 211, 8–17. https://doi.org/10.1016/j.combustflame.2019.09.019

Zhao, P., Liang, W., Deng, S., Law, C.K., 2016. Initiation and propagation of laminar premixed cool flames. Fuel 166, 477–487. https://doi.org/10.1016/j.fuel.2015.11.025

Zhou, M., Lee, M., Ju, Y., Suzuki, Y., 2025. Spatial distribution and temporal evolution of wall-stabilized DME/O2 premixed cool flames. Combust. Flame 271, 113814. https://doi.org/10.1016/j.combustflame.2024.113814

Zhu, H., Huang, Y., Yin, S., Zhang, W., 2024. Microwave plasma setups for CO2 conversion: A mini-review. Green Energy Resour. 2, 100061. https://doi.org/10.1016/j.gerr.2024.100061

Highlights:

- Turbulent cool flame structures are modified (lifted) by methane addition through the decline of cool flame extinction limits.
- The different flame regions associated with differing thermochemical characteristics for the dual-fuel lifted cool flames are uncovered.
- Methane addition inhibits the DME low-temperature oxidation.
- The kinetic mechanisms behind are identified: CH_4 competes with the DME H-abstraction reaction for OH radicals and the reaction of QOOH <=> O_2 + $2CH_2O$ is significantly slowed down with the methane addition.

Declaration of interests

☒ The authors declare that they have no known competing financial interests or personal relationships that could have appeared to influence the work reported in this paper.

☐ The authors declare the following financial interests/personal relationships which may be considered as potential competing interests: